Math. Model. Nat. Phenom. 16 (2021) 46
https://doi.org/10.1051/mmnp/2021036

Mathematical Modelling of Natural Phenomena
www.mmnp-journal.org

CONTROL OF TRAVELING LOCALIZED SPOTS*

S. Martens[1], C. Ryll[2], J. Löber[1,3], F. Tröltzsch[2] and H. Engel[1,**]

Abstract. Traveling localized spots represent an important class of self-organized two-dimensional patterns in reaction–diffusion systems. We study open-loop control intended to guide a stable spot along a desired trajectory with desired velocity. Simultaneously, the spot's concentration profile does not change under control. For a given protocol of motion, we first express the control signal analytically in terms of the Goldstone modes and the propagation velocity of the uncontrolled spot. Thus, detailed information about the underlying nonlinear reaction kinetics is unnecessary. Then, we confirm the optimality of this solution by demonstrating numerically its equivalence to the solution of a regularized, optimal control problem. To solve the latter, the analytical expressions for the control are excellent initial guesses speeding-up substantially the otherwise time-consuming calculations.

Mathematics Subject Classification. 35B06, 35C07, 93C10, 49M41, 35Q93.

Received October 7, 2020. Accepted June 10, 2021.

1. Introduction

Localized spots, sometimes referred to as auto-solitons [22], dissipative solitons [39], or bumps [24], are a subclass of traveling waves that spontaneously evolve in two-dimensional (2D) dissipative nonlinear systems driven far from thermodynamic equilibrium. In a co-moving reference frame, spots are stationary solutions to coupled nonlinear partial differential equations (PDE), such as reaction–diffusion (RD) or neural field equations, for example. The characteristic length and time scales of the spots, *i.e.*, their wave profile, propagation velocity, etc., are selected by the experimental conditions or the parameters of the model.

Experimentally, localized spots have been observed as current filaments in gas-discharge [40], as bright intensity spots in nonlinear optics and laser physics [1], as well as moving localized regions of increased concentration in chemical reactions [51] or coverage of adsorbed species in heterogeneous catalysis [53]. Further examples include temperature spots in fixed-bed catalytic reactors [52], actin conformation in dictyostelium discoideum [25], neural activity in head-direction cells [47], vegetation patterns [15], and many others.

Although control of self-organized patterns attracted considerable attention over the last decades, compare [33, 50] and references therein, it is still a challenging problem in applied nonlinear dynamics. In the context of localized spots, an illustrative applicative example are temperature spots in catalytic reactors. Transient

* Movies are available at https://www.mmnp-journal.org/.

Keywords and phrases: Pattern formation, Goldstone mode control, reaction–diffusion system, instabilities, traveling spot solutions.

[1] Institut für Theoretische Physik, Hardenbergstraße 36, EW 7-1, Technische Universität Berlin, 10623 Berlin, Germany.
[2] Technische Universität Berlin, Institut für Mathematik, Str. d. 17. Juni 136, MA 4-5, 10623 Berlin, Germany.
[3] Max-Planck-Institut für Physik komplexer Systeme, Nöthnitzer Straße 38, 01187 Dresden, Germany.

** Corresponding author: h.engel@physik.tu-berlin.de

and sustained moving hot-spot activity spontaneously formed near the wall of catalytic packed-bead and flow reversal reactors, respectively, may pose severe safety hazard problems. Another example is the control of localized neural activity including so-called bump solutions to neural field equations describing ensembles of synaptically coupled neurons [11, 24, 56]. Catalytic reactors and neural networks are only two fields where spontaneously emerging traveling spots may play a role. Other areas include gas-discharge, polymerization fronts, and solid fuel combustion.

Often, one distinguishes between open-loop, closed-loop, and optimal control. Open-loop control is independent of the instantaneous state of the system. As a consequence, it is inherently susceptible to perturbations in the initial conditions as well as to parameter uncertainty. Thus, detailed knowledge of the system's dynamics and in-depth stability analysis are pre-conditions for reliable open-loop schemes. Typical examples of open-loop control are space-time dependent external forcing [10, 58] or control by imposed geometric constraints [19, 57]. On the other hand, in closed-loop or feedback control, the controlled state is permanently monitored to adjust the control signal accordingly [23, 30, 38]. Particularly, time-delayed feedback can induce pattern forming instabilities in addition to the pattern to be controlled [16].

Optimal control reformulates control problems in terms of the minimization of a cost functional [5, 20]. Often, as in our paper, the cost functional measures the distance in function space between a desired target state and the actual controlled state of the system. If a control signal is the unique solution to an optimal control problem, then no other control, be it open- or closed-loop, will be able to enforce a controlled state closer to the target state. For nonlinear models, the uniqueness of optimal controls is a difficult and mathematically widely open issue. If an optimal control satisfies a second-order sufficient optimality condition, then it is at least locally unique, *i.e.*, it delivers an isolated minimum; we refer to [2, 9]. Optimal control of self-organized patterns requires complete knowledge of the PDEs governing the system's evolution in time and space. Numerical solutions to optimal control of PDEs often base on computationally expensive iterative algorithms. The convergence to the target state can sensitively depend on an appropriate initial guess for the control signal.

For traveling wave patterns, a general control task is position control aimed at guiding the pattern according to a given *protocol of motion* (POM), *i.e.*, moving it with desired velocity along a desired trajectory through a spatial domain. In some technical applications like catalytic reactors, it is necessary to avoid the collision of high-temperature spots with the reactor walls or their pinning at heterogeneities of the catalyst's support to maintain operational safety [52]. Another example of open-loop position control is the enhancement of the CO_2 production rate during the low-pressure catalytic oxidation of CO on Pt(110) single crystal surfaces by dragging reaction pulses and fronts using a focused laser beam with a speed differing from their natural propagation velocity in the absence of control [41, 54]. In a photosensitive Belousov-Zhabotinsky (BZ) medium, periodic variation of the applied light intensity can force a spiral wave tip to describe a wide range of hypocycloidal and epicycloidal trajectories [45, 46]. In optical bistable media like dye-doped liquid crystals and Kerr cavities, interface dynamics can be controlled by spatially inhomogeneous forcing [37]. Position control of traveling wave patterns can be tackled by feedback control as well. For example, the spiral wave core in a photosensitive BZ medium was steered around obstacles using feedback signals obtained from wave activity measured at a point detector, from tangential crossing of wavefronts with detector lines, or from a spatially extended control domain [44, 58, 59]. Two feedback loops were used to stabilize and guide unstable traveling wave segments along pre-given trajectories [43]. Furthermore, feedback-mediated control loops were employed to prevent transversal instabilities in reaction–diffusion waves [48].

Recently, we proposed an open-loop control method that acts solely via the Goldstone modes of wave patterns [26] and, therefore, can be referred to as *Goldstone mode control*. The method provides analytical expressions for the amplitude of the control signal to be applied for a given POM. We demonstrated that this control is able to accelerate or decelerate 1D traveling front and pulse solutions to RD equations [4, 26, 27] without changing their spatial profile. The stability of the control loop with respect to small changes in the initial conditions was discussed in [28]. Goldstone mode control also applies to move the core of a spiral wave at desired velocity along a pre-given trajectory through a 2D spatial domain, or to shape iso-concentration lines of 2D traveling pulses [29]. Interestingly enough, the control turned out to be equivalent to the solution of an appropriately formulated optimal control problem [26, 42].

In this paper, we extend Goldstone mode control to spatially localized moving spots. We introduce a three-component RD model supporting stable traveling spot solutions in Section 2 and derive analytical expressions for position and orientation control of traveling spots in the fully-actuated case in Section 3.1. The corresponding optimal control problem with an objective functional involving a Tikhonov regularization term is formulated explicitly in Section 3.2. Here, we discuss the relation between Goldstone mode control derived in Section 3.1 and the solutions to the optimal control problem. In Section 4, after a brief description of the numerical methods being used, we discuss examples for fully-actuated position and orientation control of spots in Sections 4.1 and 4.2, respectively, as well as for under-actuated position control by a single control signal 4.3. Summarizing, in Section 5 we conclude that our control method will be applicable if symmetry induced Goldstone modes exist as a consequence of translational and rotational invariance of the underlying evolution equation. Additionally, in the spectrum of the linear stability operator of the uncontrolled stable solution a sufficiently large gap should exist between the symmetry-induced neutral eigenvalues on the imaginary axis and the remaining eigenvalues with negative real part.

2. Three-component spot model

Throughout this work, we consider the following three-component RD system exhibiting immobile and traveling stable spot solutions in 2D [13, 39, 49]

$$\begin{aligned}
\partial_t u(\mathbf{r},t) =& D_u \Delta u + \kappa_2\, u - u^3 - \kappa_3 v - \kappa_4 w + \kappa_1, && \text{(2.1a)}\\
\tau \partial_t v(\mathbf{r},t) =& D_v \Delta v + u - v, && \text{(2.1b)}\\
\theta \partial_t w(\mathbf{r},t) =& D_w \Delta w + u - w, \quad \mathbf{r}\in\Omega. && \text{(2.1c)}
\end{aligned}$$

Here, $\Delta = \partial_x^2 + \partial_y^2$ represents the Laplacian in Cartesian coordinates, $\mathbf{r}$ is the position vector in the spatial domain Ω, $\mathbf{r} = (x,y)^T \in \Omega \subset \mathbb{R}^2$, and t indicates time. D_u, D_v, and D_w denote the diffusion coefficients of components u, v, and w while τ and θ set the time scales for the v and w kinetics, respectively. Beside spots, the model (2.1) is capable to support peanut patterns [36], breathing solitons [17], and jumping oscillons [55], for example.

Model (2.1) is an extension of the well-known FitzHugh-Nagumo model [14]. It was first introduced by Purwins and co-workers to describe the dynamics of current filaments in planar gas-discharge [39]. In this context, activator u and inhibitor v represent the current density and the voltage drop over the high-ohmic electrode, respectively. The second inhibitor w is linked to the surface charge, and the additive parameter κ_1 is related to the supply voltage.

In a more general interpretation, the model (2.1) represents a RD system of activator-inhibitor type with cubic nonlinearity. Two inhibiting components couple linearly with linear kinetics into the equation of the activator component. In a propagating spot, the inhibitor v is delayed with respect to the activator u, *i.e.*, the center of the u and v concentration fields do not lay on top of each other. In contrast, because of its small time constant θ and large diffusion coefficient, inhibitor w quickly follows the activator distribution and surrounds it entirely. This second inhibitor stabilizes the moving spot. Altogether, (2.1) define a minimal model for traveling 2-D spot solutions.

3. Controlling position and orientation of traveling spots

3.1. Analytical expression for control amplitudes in position control

Let us consider a controlled RD system according to

$$\partial_t \mathbf{U}(\mathbf{r},t) - \mathbb{D}\Delta\mathbf{U}(\mathbf{r},t) - \mathbf{R}(\mathbf{U}(\mathbf{r},t)) = \mathbb{B}\mathbf{f}(\mathbf{r},t). \qquad \text{(3.1a)}$$

Here, $\mathbf{U}(\mathbf{r},t) = (u_1(\mathbf{r},t),\dots,u_n(\mathbf{r},t))^T$ is the vector of $n \in \mathbb{N}$ state components defined in the two-dimensional spatial domain $\Omega \subset \mathbb{R}^2$ with $\mathbf{r} = (x,y)^T$. Assuming an isotropic medium, the $n \times n$ matrix of diffusion coefficients $\mathbb{D}$ is diagonal and constant, $\mathbb{D} = \mathrm{diag}(D_1,\dots,D_n)$. The vector $\mathbf{R}(\mathbf{U}) = (R_1(\mathbf{U}),\dots,R_n(\mathbf{U}))^T$ describes the reaction kinetics of the components. In general, $R_i(\mathbf{U})$ are nonlinear functions of the state. For the RD system (2.1), $\mathbf{U}$, $\mathbb{D}$, and $\mathbf{R}$ are given by $\mathbf{U} = (u,v,w)^T$, $\mathbb{D} = \mathrm{diag}(D_u, D_v/\tau, D_w/\theta)$, and $\mathbf{R} = \big(\kappa_2\, u - u^3 - \kappa_3 v - \kappa_4 w + \kappa_1, (u-v)/\tau, (u-w)/\theta\big)^T$, respectively. Equation (3.1a) must be supplemented with an initial condition

$$\mathbf{U}(\mathbf{r},t_0) = \mathbf{U}_0(\mathbf{r}), \tag{3.1b}$$

and appropriate boundary conditions. We consider a rectangular domain $\Omega = (x_a,x_b] \times (y_a,y_b]$ with periodic boundary conditions such that $\mathbf{U}$ as well as its derivatives in the direction normal to the boundary are periodic,

$$\begin{aligned} \mathbf{U}(x_a,y,t) &= \mathbf{U}(x_b,y,t), & \frac{\partial}{\partial x}\mathbf{U}(x_a,y,t) &= \frac{\partial}{\partial x}\mathbf{U}(x_b,y,t), \\ \mathbf{U}(x,y_a,t) &= \mathbf{U}(x,y_b,t), & \frac{\partial}{\partial y}\mathbf{U}(x,y_a,t) &= \frac{\partial}{\partial y}\mathbf{U}(x,y_b,t). \end{aligned} \tag{3.1c}$$

The space-time dependent control signals $\mathbf{f}(\mathbf{r},t) = (f_1(\mathbf{r},t),\dots,f_m(\mathbf{r},t))^T$, $m \in \mathbb{N}$, on the right hand side of (3.1a) are assumed to act for all times t everywhere within Ω.

The constant $n \times m$ matrix $\mathbb{B}$ determines which components are directly affected by the control signals. A system with strictly less independent control signals than components, $m < n$, is *underactuated*. For $m = n$ and $\mathbb{B}$ invertible, the system is *fully actuated*. In what follows, we focus on fully actuated systems and set $\mathbb{B}$ equal to the identity matrix $\mathbb{1}$. The limiting case of single component control, *i.e.*, $\mathbb{B}\mathbf{f}(\mathbf{r},t) \propto (f_1(\mathbf{r},t),0,\dots,0)^T$, we consider in subsection 4.3.

The partial differential equations (3.1a) describe the evolution of the components $\mathbf{U}(\mathbf{r},t)$ in the presence of spatio-temporal perturbations $\mathbf{f}(\mathbf{r},t)$ that break the translation and rotation invariance of the unperturbed equations. In this interpretation, the response of the unperturbed solution to a given small input $\mathbf{f}$ can be calculated perturbatively, see references [3, 34, 35], and Appendix C.2.

In this paper, however, following [26] we perceive (3.1a) for given desired spot dynamics as a conditional equation for the perturbations which now are considered as control inputs. The goal of the control $\mathbf{f}$ is to enforce a state $\mathbf{U}$ to follow a given *desired distribution* $\mathbf{U}_d(\mathbf{r},t) = (u_{1,d}(\mathbf{r},t),\dots,u_{n,d}(\mathbf{r},t))^T$ as closely as possible everywhere in the spatial domain Ω and for all times $0 \le t \le T$. We call a desired distribution $\mathbf{U}_d$ *exactly realizable* if there exists a control $\mathbf{f}$ such that the controlled state $\mathbf{U}$ equals $\mathbf{U}_d$ everywhere in the space-time cylinder $Q = \Omega \times [0,T]$.

Inserting $\mathbf{U}_d$ for $\mathbf{U}$ in (3.1a) yields for the control

$$\mathbf{f}(\mathbf{r},t) = \mathbb{B}^{-1}\{\partial_t \mathbf{U}_d(\mathbf{r},t) - \mathbb{D}\Delta\mathbf{U}_d(\mathbf{r},t) - \mathbf{R}(\mathbf{U}_d(\mathbf{r},t))\}. \tag{3.2}$$

For $\mathbf{U}_d$ to be exactly realizable, three more conditions must be satisfied: First, the initial condition for the controlled state, (3.1b), must coincide with the initial state of the desired distribution, $\mathbf{U}(\mathbf{r},0) = \mathbf{U}_d(\mathbf{r},0)$. Second, all boundary conditions for the desired distribution $\mathbf{U}_d$ have to comply with the boundary conditions for $\mathbf{U}$, (3.1c). Third, $\mathbf{U}_d$ must be sufficiently smooth in the space-time cylinder $Q = \Omega \times [0,T]$ such that the derivatives $\partial_t \mathbf{U}_d$ and $\Delta\mathbf{U}_d$ are continuous. The construction of such desired distributions is difficult and hence this method of control is not practicable. It is more convenient to control certain patterns that are asymptotic solutions of the uncontrolled system (3.1) for $t \to \infty$ in the space $\mathbb{R}^2$, for instance spot solutions.

Therefore, we formulate the control goal for spot solutions to the uncontrolled RD equations (3.1). These solutions propagate with constant velocity $\mathbf{v}_0 = (v_0^x, v_0^y)^T$ and wave profile $\mathbf{U}_c$ through the spatial domain. In

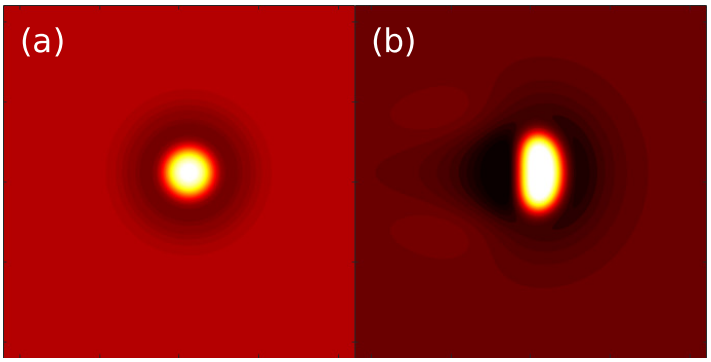

FIGURE 1. Activator distribution u of a rotational symmetric resting (a) and an axis-symmetric traveling spot solution (b) to (2.1). Parameters $\kappa_1 = -5.0$, $\tau = 2$ in (a) and $\kappa_1 = -6.92$, $\tau = 48$ in (b); remaining parameters are taken from set 1 in Table 1. In both panels, identical domain size and colormap are used.

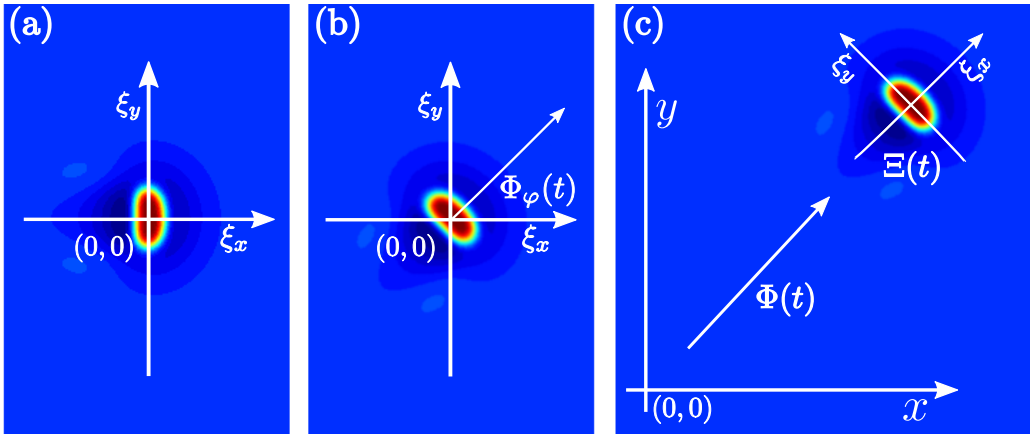

FIGURE 2. Position and orientation of the spot $\mathbf{U}_d(\mathbf{r},t)$ as defined in (3.4). (a) Wave profile of the activator distribution, $U_c(\boldsymbol{\xi})$, centered in the co-moving and co-rotating frame of reference at $\boldsymbol{\xi} = (0,0)^T$. (b) Counter-clockwise rotation of $U_c(\boldsymbol{\xi})$ according to the desired orientation $\Phi_\varphi(t)$. (c) Shift of the rotated solution in virtue of the translational protocol of motion $\boldsymbol{\Phi}(t) = (\Phi_x(t), \Phi_y(t))^T$.

a co-moving frame of reference, $\boldsymbol{\xi} = (\xi_x, \xi_y)^T \equiv \mathbf{r} - \mathbf{v}_0 t$, $\mathbf{U}_c$ satisfies the equation

$$\mathbf{0} = \mathbb{D}\Delta_{\boldsymbol{\xi}}\mathbf{U}_c(\boldsymbol{\xi}) + \mathbf{v}_0 \cdot \nabla_{\boldsymbol{\xi}}\mathbf{U}_c(\boldsymbol{\xi}) + \mathbf{R}(\mathbf{U}_c(\boldsymbol{\xi})), \tag{3.3}$$

where, $\nabla_{\boldsymbol{\xi}} = (\partial_{\xi_x}, \partial_{\xi_y})^T$ and $\Delta_{\boldsymbol{\xi}} = \partial^2_{\xi_x} + \partial^2_{\xi_y}$ denote the component-wise gradient and Laplacian, respectively. We emphasize that resting localized spots, $\mathbf{v}_0 = \mathbf{0}$, are rotationally-symmetric solutions while traveling localized spots are axis-symmetric with the symmetry axis directed tangentially to the trajectory of motion, *cf.* Figure 1a and b, respectively. We characterize the current position of a spot by the x- and y-coordinates of the maximum value of the activator concentration along its symmetry axis at a given time, $\boldsymbol{\Phi}(t) = (\Phi_x(t), \Phi_y(t))^T$, and its orientation by the angle $\Phi_\varphi(t)$ between the spot's symmetry axis and the x-axis, compare Figure A.1.

A distribution following a prescribed POM $\boldsymbol{\Xi}(t) = (\boldsymbol{\Phi}(t), \Phi_\varphi(t))^T$, while simultaneously preserving the profile of the uncontrolled spot $\mathbf{U}_c$, reads

$$\mathbf{U}_d(\mathbf{r}, t) = \mathbf{U}_c(\mathbb{A}(-\Phi_\varphi(t))\,(\mathbf{r} - \boldsymbol{\Phi}(t))). \tag{3.4}$$

Here, $\mathbb{A}(\alpha) = [\cos(\alpha), -\sin(\alpha); \sin(\alpha), \cos(\alpha)]$ is the clockwise rotation matrix in 2D. For the desired distribution (3.4) to be exactly realizable, the initial condition must be a spot solution of the form $\mathbf{U}(\mathbf{r}, t_0) = \mathbf{U}_c(\mathbb{A}(-\phi_0)\,(\mathbf{r} - \mathbf{r}_0))$, which yields for the initial values of the POM $\boldsymbol{\Phi}(t_0) = \mathbf{r}_0$ and $\Phi_\varphi(t_0) = \phi_0$, respectively. Inserting the desired distribution (3.4) into the general control solution (3.2) leads to

$$\mathbf{f}(\mathbf{r}, t) = \left[-\left(\mathbb{A}_z(-\Phi_\varphi(t))\,\dot{\boldsymbol{\Xi}}(t)\right) \cdot \tilde{\nabla}_{\boldsymbol{\xi}} \mathbf{U}_c(\boldsymbol{\xi}) - \mathbb{D}\Delta_{\boldsymbol{\xi}} \mathbf{U}_c(\boldsymbol{\xi}) - \mathbf{R}(\mathbf{U}_c(\boldsymbol{\xi})) \right]_{\boldsymbol{\xi} = \bar{\boldsymbol{\xi}}(t)}, \tag{3.5}$$

with $\bar{\boldsymbol{\xi}}(t) = \mathbb{A}(-\Phi_\varphi(t))\,(\mathbf{r} - \boldsymbol{\Phi}(t))$. For the sake of a compact notation, we introduced the differential operator $\tilde{\nabla}_{\boldsymbol{\xi}} = (\partial_{\xi_x}, \partial_{\xi_y}, \partial_\varphi)^T$ with the angular derivative $\partial_\varphi = -\xi_y \partial_{\xi_x} + \xi_x \partial_{\xi_y}$. The dot denotes the derivative with respect to time t, and $\mathbb{A}_z(\alpha)$ is the clockwise rotation matrix around the z-axes in 3D, $\mathbb{A}_z(\alpha) = \mathrm{diag}(\mathbb{A}(\alpha), 1)$. Using equation (3.3) for the uncontrolled spot profile, we end up with the expression

$$\mathbf{f}_{\mathrm{Gold}}(\mathbf{r}, t) = \left[\left(\begin{pmatrix} v_0^x \\ v_0^y \\ 0 \end{pmatrix} - \mathbb{A}_z\left(-\Phi_\varphi(t)\right) \begin{pmatrix} \dot{\Phi}_x(t) \\ \dot{\Phi}_y(t) \\ \dot{\Phi}_\varphi(t) \end{pmatrix} \right) \cdot \tilde{\nabla}_{\boldsymbol{\xi}} \right] \mathbf{U}_c(\boldsymbol{\xi}) \Big|_{\boldsymbol{\xi} = \bar{\boldsymbol{\xi}}(t)} \tag{3.6}$$

for our Goldstone mode control (see Appendix C.2, (C.22)).

Remarkably, any reference to the nonlinear functions $\mathbf{R}$ drops out from the result (3.6). This is of great advantage in all applications where the details of the underlying reaction kinetics $\mathbf{R}$ are largely unknown or difficult to identify. Once propagation velocity $\mathbf{v}_0$ and wave profile $\mathbf{U}_c$ of the uncontrolled spot are measured with an accuracy sufficient to calculate the Goldstone modes $\partial_{\xi_x} \mathbf{U}_c$, $\partial_{\xi_y} \mathbf{U}_c$, and $\partial_\varphi \mathbf{U}_c$, the control signals can be computed in advance for the complete time interval $[0, T]$. Consequently, in contrast to feedback control, a continuous recording of the system is not required.

One notices that (3.6) equals the sum of Goldstone modes with time-dependent prefactors, $\mathbf{f}_{\mathrm{Gold}}(\mathbf{r}, t) = P_1(t)\,\partial_{\xi_x} \mathbf{U}_c(\boldsymbol{\xi}) + P_2(t)\,\partial_{\xi_y} \mathbf{U}_c(\boldsymbol{\xi}) + P_3(t)\,\partial_\varphi \mathbf{U}_c(\boldsymbol{\xi})$. The Goldstone modes are the right eigenvectors to the linear stability operator $\mathcal{L}$ of (3.3)

$$\mathcal{L} = \mathbb{D}\Delta_{\boldsymbol{\xi}} + \mathbf{v}_0 \cdot \nabla_{\boldsymbol{\xi}} + \mathcal{D}\mathbf{R}(\mathbf{U}_c\,(\boldsymbol{\xi})), \tag{3.7}$$

to the eigenvalue zero. They are associated with the translational and rotational invariance of equation (3.1a) in $\mathbb{R}^2$ for $\mathbf{f}(\mathbf{r}, t) = 0$. Clearly, the prefactors' magnitudes are proportional to the difference between the intrinsic velocity, $\mathbf{v}_0$, and the current prescribed spot velocity projected onto the x- and y-axes. If the prescribed POM $\boldsymbol{\Xi}(t)$ coincides with the spot's natural motion, then all prefactors vanish identically and $\mathbf{f}_{\mathrm{Gold}}$ disappears everywhere in Q. Importantly, the control signal is localized around the spot position and vanishes far from it because the spatial derivatives of its profile decay sufficiently fast, $\lim_{\|\boldsymbol{\xi}\| \to \infty} \nabla_{\boldsymbol{\xi}} \mathbf{U}_c = \mathbf{0}$.

Alongside with these advantages, limitations in the applicability of Goldstone mode control (3.6) exist as well. For instance, the magnitude of the applied control may locally attain values that are unfeasible to realize physically because $\mathbf{f}_{\mathrm{Gold}}$ is proportional to the slope of the wave profile $\mathbf{U}_c$. Additionally, the stability of the control scheme depends sensitively on how precise the Goldstone modes can be calculated. Further, the complete spatial domain Ω accessible by the spot has to be available for the control as well. As already mentioned above, $\mathbf{f}_{\mathrm{Gold}}$ cannot be applied to desired trajectories $\mathbf{U}_d$ which do not comply with initial as well as boundary conditions or which are non-smooth. In contrary, optimal control can deal with many of these complications. An arbitrary (even non-smooth) desired distribution U_d is approximated as close as possible by a control f that has to

be found by numerical optimization. However, optimal control is computationally much more expensive than Goldstone mode control.

If the desired $\mathbf{U}_d$ is not realizable by some control $\mathbf{f}$, then the method of this subsection is not applicable. In this case, an optimal control problem can be solved that determines the best approximation of Ud in the $L^2(Q)$-norm. This is the issue of the next subsection.

3.2. Optimal control

An optimal control $\mathbf{f}$ minimizes a so-called *objective functional* J that is in our case of tracking-type

$$J(\mathbf{U},\mathbf{f}) = \frac{1}{2}\sum_{i=1}^{3}\left[\int_0^T\!\!\int_\Omega (u_i - u_{i,d})^2 \,\mathrm{d}\mathbf{r}\,\mathrm{d}t + \nu \int_0^T\!\!\int_\Omega f_i^2 \mathrm{d}\mathbf{r}\,\mathrm{d}t\right]. \tag{3.8}$$

$\mathbf{U}$ satisfies the controlled state equation associated to $\mathbf{f}$ with respect to given initial and boundary conditions, *cf.* equations (3.1). The first term appearing in J measures the distance between the actual and the desired solution $\mathbf{U}$ and $\mathbf{U}_d$ up to the terminal time T in an $L^2(Q)$-sense. In the second, so-called Tikhonov regularization term, a small positive number ν guarantees the existence of an optimal control $\mathbf{f}_{\mathrm{opt}}$ that minimizes the objective functional (3.8) for $\Omega \subset \mathbb{R}^q, q = 1, 2, 3$, see reference [6]. If the desired state $\mathbf{U}_d$ is not exactly realizable and $\nu = 0$, then the functional (3.8) would not have a minimum. Then the optimal control problem is unsolvable. However, for any exactly realizable desired state $\mathbf{U}_d$ and $\nu = 0$, the solution $\mathbf{f}$ to (3.2) is the optimal control for (3.8). If $\mathbf{U}_d$ is not exactly realizable, then an approximation of $\mathbf{U}_d$ is obtained as part of the solution to the optimal control problem.

The minimization of J must be performed with respect to state $\mathbf{U}$ and control $\mathbf{f}$. Expressing $\mathbf{U}$ in terms of $\mathbf{S}(\mathbf{f})$, where $\mathbf{S} : \mathbf{f} \mapsto \mathbf{U}$ is the solution operator to (3.1) in Q, justifies the definition of a reduced objective functional $J(\mathbf{f}) := J(\mathbf{S}(\mathbf{f}), \mathbf{f})$. In order to minimize J by a descent method, its first directional derivative with respect to $\mathbf{f}$ in the direction $\mathbf{h}$ is needed that can be determined by the chain rule

$$J'(\mathbf{f})\mathbf{h} = \int_0^T\!\!\int_\Omega ((\mathbf{S}(\mathbf{f})) - \mathbf{U}_d) \cdot (\mathbf{S}'(\mathbf{f})\mathbf{h}) \,\mathrm{d}\mathbf{r}\,\mathrm{d}t + \nu \int_0^T\!\!\int_\Omega \mathbf{f}\cdot\mathbf{h}\,\mathrm{d}\mathbf{r}\,\mathrm{d}t\,. \tag{3.9}$$

The state $\mathbf{U}$ is constrained to satisfy the controlled state equation together with given initial and boundary conditions, *cf.* equations (3.1). By a Lagrange multiplier $\mathbf{P}(\mathbf{r},t) = (p_1(\mathbf{r},t),\ldots,p_n(\mathbf{r},t))^T$, also called the *adjoint state*, the state equation can be "eliminated" to simplify (3.9),

$$J'(\mathbf{f})\mathbf{h} = \int_0^T\!\!\int_\Omega (\mathbf{P} + \nu\,\mathbf{f})\cdot\mathbf{h}\,\mathrm{d}\mathbf{r}\,\mathrm{d}t\,. \tag{3.10}$$

The adjoint state $\mathbf{P}$ is the solution of the *adjoint equation*

$$-\partial_t\mathbf{P}(\mathbf{r},t) - \mathbb{D}\Delta\mathbf{P}(\mathbf{r},t) - \mathcal{D}\mathbf{R}^T(\mathbf{U}(\mathbf{r},t))\mathbf{P}(\mathbf{r},t) = \mathbf{U} - \mathbf{U}_d \quad \text{in} \quad Q, \tag{3.11}$$

subject to terminal condition $\mathbf{P}(\cdot,T) = \mathbf{0}$ in Ω and periodic boundary conditions in $\partial\Omega$, where $\mathcal{D}\mathbf{R}^T$ denotes the transposed Jacobian matrix of $\mathbf{R}$ with respect to $\mathbf{U}$. In the minimum, *i.e.*, for an optimal control $\mathbf{f} = \mathbf{f}_{\mathrm{opt}}$ with state $\mathbf{U} = \mathbf{U}_{\mathrm{opt}}$ and adjoint state $\mathbf{P} = \mathbf{P}_{\mathrm{opt}}$, the derivative $J'(\mathbf{f}_{\mathrm{opt}})\mathbf{h}$ has to be zero in all directions $\mathbf{h}$. In view of (3.10), it is rather obvious that this amounts to

$$\mathbf{P}_{\mathrm{opt}} + \nu\,\mathbf{f}_{\mathrm{opt}} = \mathbf{0}. \tag{3.12}$$

TABLE 1. Parameter values used in the numerical simulations. The parameters $\theta = 1$, $\kappa_2 = 2$, $\kappa_3 = 1$, and $\kappa_4 = 8.5$ are the same for set 1 and set 2.

	D_u	D_v	D_w	τ	κ_1	v_0^x
Set 1	1.0×10^{-4}	1.86×10^{-4}	9.6×10^{-3}	48.0	-6.92	2.599×10^{-3}
Set 2 [36]	0.9×10^{-4}	1.00×10^{-3}	1.0×10^{-2}	40.0	-7.30	1.776×10^{-3}

This is nothing more than the well-known condition that, in a minimum, the gradient of the function to be minimized is zero.

Due to the mixed initial and terminal conditions for $\mathbf{U}$ and $\mathbf{P}$, it is rarely possible to find numerical solutions to optimal control by a direct integration method. To reduce numerical costs, we employ Model Predictive Control and split our optimal control problem in subproblems with a 4 time-step small time-horizon [42]. Thereby, each subproblem is solved with a gradient or conjugate gradient optimization method that employs formula (3.10) for gradient computations. We refer to [4, 7] for the optimal control of traveling wave fronts or spiral waves and to [8] for optimal control of localized spots. Details on the iteration scheme are discussed in the supplementary information (SI), paragraph S1.

4. EXAMPLES

In the following, we discuss three examples for position control of traveling spot solutions to the three-component RD model (2.1). Mainly, we compare Goldstone mode control $\mathbf{f}_{\text{Gold}}$ with optimal control $\mathbf{f}_{\text{opt}}$. If not stated otherwise, the state equation (3.1a) and the adjoint equation (3.11) are solved on a squared domain $\Omega = (-0.5, 0.5] \times (-0.5, 0.5]$ with periodic boundary conditions (3.1c) both in x and y. The domain size is sufficiently large to avoid self-interaction of the spots in the periodic simulation domain. Without loss of generality, we fix the spot's direction of motion to coincide with the x-axis, *i.e.*, $v_0^x \neq 0$ and $v_0^y = 0$. Any numerical simulation of equation (3.1a) is initialized with the profile $\mathbf{U}_c$ of the uncontrolled spot. This profile and the corresponding natural velocity $\mathbf{v}_0$ are obtained by solving the nonlinear eigenvalue problem (3.3) with adequate accuracy. Further details on the used numerical methods, the spatial and temporal resolution, and the initial conditions are presented in Appendix A.1.

4.1. Translational position control of spots

In our first example, we aim to shift the spot's position along a Lissajous curve without controlling its orientation, *i.e.*, the spot's symmetry axis is kept frozen to the x-axis. Thus, the POM $\boldsymbol{\Xi}(t) = (\Phi_x(t), \Phi_y(t), \Phi_\varphi(t))^T$ is given by

$$\Phi_x(t) = r\,\sin(4\pi\, t/T)), \quad \Phi_y(t) = r\,\sin(6\pi\, t/T)), \quad \text{and} \quad \Phi_\varphi(t) = 0, \tag{4.1}$$

with radius $r = 0.2$ and protocol duration $T = 200$. The video [SI_video1] shows the complete dynamics of all three state components $\mathbf{U}$ as well as $\mathbf{f}_{\text{Gold}}$ and $\mathbf{f}_{\text{opt}}$. In Figure 3a, we depict the time evolution of the activator distribution $u(\mathbf{r}, t)$ under the action of the control $\mathbf{f}_{\text{Gold}}$ shown in Figure 3b. The spot follows the desired trajectory indicated by the dashed line. The orientation of its symmetry axis remains fixed while the control signal realigns at any instant of time. Indeed, in the absence of orientation control, $\Phi_\varphi(t) = 0$, $\mathbf{f}_{\text{Gold}}$ can be expressed by the projection of $\nabla \mathbf{U}_c$ onto the tangential vector to the Lissajous curve $\mathbf{T}(t)$, $\mathbf{f}_{\text{Gold}}(\mathbf{r}, t) = \left[\left(v_0^x - \dot{\Phi}_x(t)\right) \partial_{\xi_x} \mathbf{U}_c\left(\boldsymbol{\xi}(t)\right) - \dot{\Phi}_y(t) \partial_{\xi_y} \mathbf{U}_c\left(\boldsymbol{\xi}(t)\right)\right] \propto \mathbf{T}(t) \cdot \nabla\, \mathbf{U}_c$, with $\boldsymbol{\xi}(t) = \mathbf{r} - \boldsymbol{\Phi}(t)$. Obviously, the control is localized at the current spot position $\boldsymbol{\Phi}(t)$ and vanishes far away from it. Despite that the average speed $\bar{v} = L_{\text{curve}}/T \approx 6 v_0^x$ along the studied Lissajous curve (4.1) with arc length L_{curve} is almost five times larger than the propagation velocity of the uncontrolled spot, the magnitude of $f_{u,\text{Gold}}$ is of the same order as the

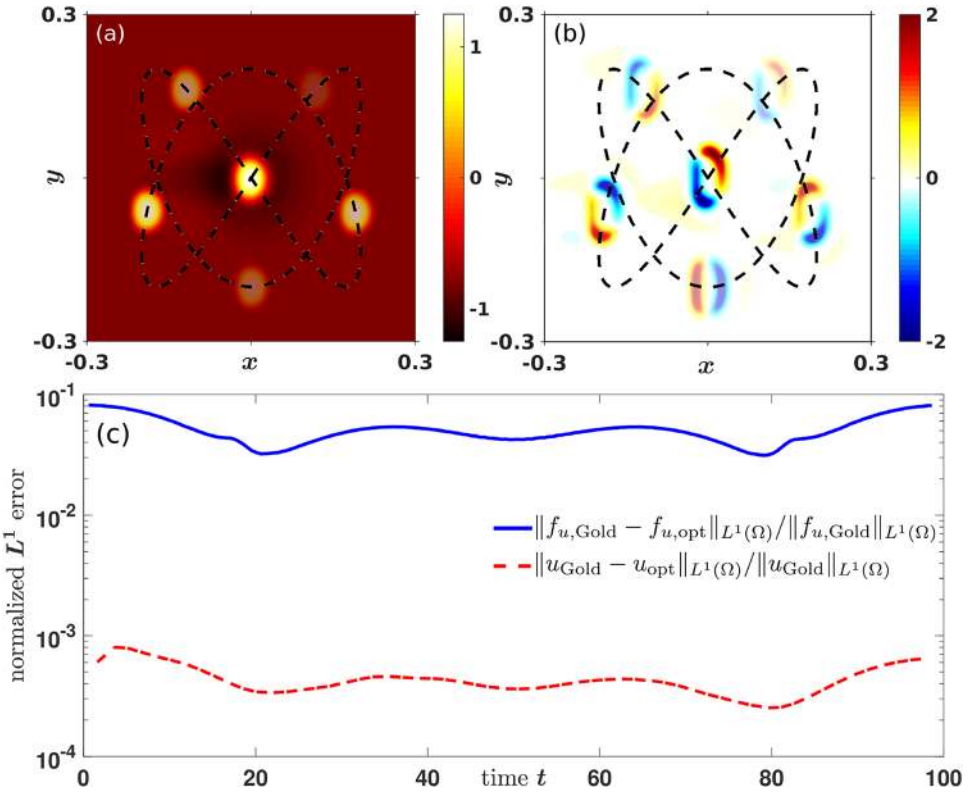

FIGURE 3. Position control along the Lissajous curve (4.1), see [SI_video1]. (a) Snapshots of the activator distribution $u(\mathbf{r}, t)$ obtained from numerical simulation of (2.1)–(3.1a) with control $\mathbf{f}_{\mathrm{Gold}}$, (3.6), at time moments $t = \{10, 50, 90, 130, 170, 200\}$. (b) Control $f_{u,\mathrm{Gold}}(\mathbf{r}, t)$ at the same instants of time. In (a) and (b), the dark dashed line indicates the Lissajous curve and the decreasing transparency marks consecutive time moments. (c) Temporal behavior of the relative $L^1(\Omega)$ error (4.2) between $f_{u,\mathrm{Gold}}$ (3.6), and optimal activator control signals $f_{u,\mathrm{opt}}$ (3.8) during $t \in [0, T/2]$. We select set 1 in Table 1 for the parameters to (2.1) and set the Tikhonov parameter to $\nu = 10^{-7}$.

local reaction terms (2.1). The control signals applied to the inhibitors v and w are one and two magnitudes smaller [SI_video1] than the activator's control, respectively.

Graphically, there is no distinguishable difference between $\mathbf{f}_{\mathrm{Gold}}$ and $\mathbf{f}_{\mathrm{opt}}$, compare [SI_video1]. Both are always localized close to the current spot position, and their magnitudes change proportional to $|\dot{\mathbf{\Phi}}(t)|$. For a quantitative comparison, we compute the relative errors between $f_{u,\mathrm{Gold}}$ and $f_{u,\mathrm{opt}}$ measured by the $L^1(\Omega)$-norm

$$\|h(t)\|_{L^1(\Omega)} = \int_{\Omega} |h(\mathbf{r}, t)| \mathrm{d}\mathbf{r}\,. \tag{4.2}$$

Here, $|h(\mathbf{r}, t)|$ indicates the absolute value of h at position $\mathbf{r}$ and time t.

In Figure 3c, we depict solely the normalized error for the first half of the protocol because it starts to repeat after $T/2$, $\Phi_y(t) = -\Phi_y(t + T/2)$. The relative error between $f_{u,\mathrm{Gold}}$ and optimal control $f_{u,\mathrm{opt}}$ (solid line) ranges between 2% and 8%. As reported in Appendix A.1, the limiting error is dominated by the time step chosen in the implicit Euler scheme. Albeit the scheme is A-stable, the error at a specific time t is of the order

of $\mathcal{O}(\mathrm{d}t)$. Consequently, we observe that $\|f_{u,\mathrm{Gold}}(t) - f_{u,\mathrm{opt}}(t)\|_{L^1(\Omega)}$ is bounded from above by $\mathrm{d}t$; $\mathrm{d}t = 0.1$ in the studied example.

The dashed line in Figure 3c shows the relative error between the activator distribution obtained by Goldstone mode control and the one calculated under optimal control, $\|u_{\mathrm{Gold}}(t) - u_{\mathrm{opt}}(t)\|_{L^1(\Omega)}/\|u_{\mathrm{Gold}}(t)\|_{L^1(\Omega)}$. At any time, this error is less than 10^{-3}, *i.e.*, both controlled states agree remarkably well, despite that $\|f_{u,\mathrm{Gold}}(t) - f_{u,\mathrm{opt}}(t)\|_{L^1(\Omega)}$ is of the order 10^{-1}. Additionally, the relative errors between the desired distribution $\mathbf{U}_d$ and the state solutions $\mathbf{U}_{\mathrm{Gold}}$ and $\mathbf{U}_{\mathrm{opt}}$ are less than 10^{-7} in both cases (not shown explicitly). This confirms that the Goldstone mode control (3.6), within numerical accuracy, is indeed the solution to the corresponding unregularized optimal control problem. Similar conclusions had been obtained in our previous study of position control of front solutions in one spatial dimension, see [42].

The gradient-type method, used to solve the optimal control problem, relies on an initial guess for the control signal. The closer the starting guess is to the final solution, the fewer iteration steps are necessary to converge for most established optimization methods. Starting every iteration with an initial zero control, it takes on average $\bar{n}_{\mathrm{iter}} \simeq 23$ iterations per time step for position control along the Lissajous curve (4.1). Using the control solution of the previously solved subproblem as initial guess reduces the average number of iterations to $\bar{n}_{\mathrm{iter}} \simeq 14$. Taking advantage of the similarity between $\mathbf{f}_{\mathrm{Gold}}$ and $\mathbf{f}_{\mathrm{opt}}$, see Figure 3c, the computational costs reduce even further. The most substantial computational speed-up is obtained by initiating every optimization subproblem with (3.2). Then, the iteration stops on average after the first step, $\bar{n}_{\mathrm{iter}} \simeq 1$.

4.1.1. Stability of position control

Any open-loop controls is sensitive against perturbations of the initial conditions, data uncertainty, or numerical roundoff errors. To test the stability of our Goldstone mode control for position control $\mathbf{f}_{\mathrm{Gold}}$, we accelerate or decelerate a single spot from its initial, intrinsic velocity $\mathbf{v}_0$ to a final velocity $\mathbf{v}_1$ using a translational POM $\boldsymbol{\Xi}(t) = (\boldsymbol{\Phi}, 0)^T$ with velocity

$$\dot{\Phi}_i(t) = \begin{cases} v_0^i, & t < 0, \\ \frac{1}{2}\left((v_0^i + v_1^i) + (v_0^i - v_1^i)\,\cos\left(\pi t/T_i\right)\right), & 0 \le t \le T_i, \\ v_1^i, & t > T_i, \end{cases} \tag{4.3}$$

for $i \in \{x, y\}$. Note that both the protocol's velocity $\dot{\boldsymbol{\Phi}}(t)$ and acceleration $\ddot{\boldsymbol{\Phi}}(t)$ are continuous functions within the interval $[0, T_i]$. T_i denotes the duration of the protocol. The maximum acceleration $\pi\left(v_i^1 - v_i^0\right)/(2T_i)$ is proportional to the prescribed velocity difference $v_i^1 - v_i^0$ and inversely proportional to T_i.

A sketch of the protocol is depicted in Figure 4b. Since the proposed control scheme is an open-loop control, deviations between the current spot position $\boldsymbol{\Phi}_{\mathrm{curr}}(t)$ and the POM $\boldsymbol{\Phi}(t)$ will grow unbounded in time if the difference between them exceeds a critical value [28]. A specific protocol is called *stable* and marked by green boxes in Figure 4 if and only if the Euclidean distance is bounded as $\|\boldsymbol{\Phi}_{\mathrm{curr}}(t) - \boldsymbol{\Phi}(t)\| < L/2$ for all times $t \in [0, t_{\mathrm{end}}]$. Otherwise, it is called *unstable* (red boxes). Note that a protocol is also considered to be unstable if the control leads to the nucleation of additional spots. In order to make the results comparable for different protocol durations, we adjust the terminal simulation time t_{end} according to $t_{\mathrm{end}} = \max\left(10\,t_{\mathrm{drift}}, T_i + 10\,L/|v_1^i|\right)$ with drift time $t_{\mathrm{drift}} = L/v_0^x$. We stress that all simulation results presented in Figure 4 have been computed for sufficiently long time intervals and do not alter upon an increase of the total simulation time.

Figure 4a depicts the numerically evaluated region of stable position control (green boxes) in x-direction as a function of the ratio of terminal spot velocity v_1^x to the initial one v_0^x and the ratio of the control duration T_x to the drift time t_{drift}. The translational POM in y-direction is set to zero, $\Phi_y(t) = 0$. As expected, the numerical algorithm is stable in the absence of control, $v_1^x/v_0^x = 1$. Further, it turns out that the control scheme is mostly stable for rapid, $T_x \ll t_{\mathrm{drift}}$, to moderately slow POMs, $T_x \lesssim 10\,t_{\mathrm{drift}}$, regardless of the velocity change, $|v_1^x - v_0^x|$. The stability regions exhibit an asymmetry with respect to the sign of the velocity change. Weakly accelerating protocols, $1 < v_1^x/v_0^x \lesssim 2$, are unstable (red colored region) while decelerating ones, $v_1^x < v_0^x$, are always stable

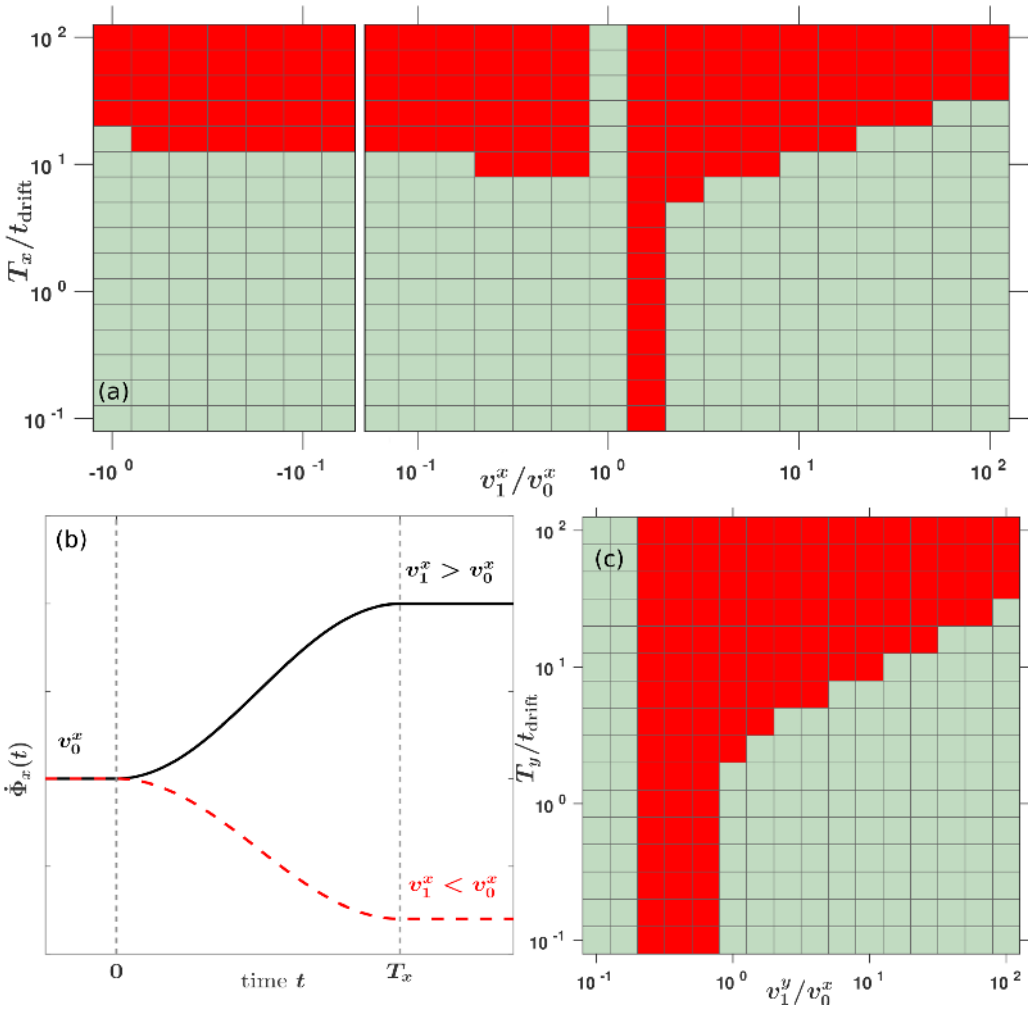

FIGURE 4. Numerically evaluated region of stability for position control $\mathbf{f}_{\text{Gold}}$. Stability (green regions) and instability (red regions) is demonstrated for an accelerating and decelerating POM (4.3) which changes the propagation velocity of a single spot from $\mathbf{v}_0$ to the final value $\mathbf{v}_1$ during T_i, $i = \{x, y\}$, see panel (b). In panel (a), the spot is exclusively accelerated or decelerated along its intrinsic direction of motion. In panel (c), the spot's propagation velocity perpendicular to the intrinsic one is controlled, $v_1^x = v_0^x$ and $v_1^y \neq 0$. The controlled spot dynamics (2.1) is simulated on a $(-0.35, 0.35] \times (-0.35, 0.35]$ domain with periodic boundary conditions using ETD2, *cf.* Appendix A.1. The system parameters are taken from set 1 in Table 1 and thus the drift time is given by $t_{\text{drift}} = L/v_0^x \approx 273$.

for $T_x \lesssim 10\, t_{\text{drift}}$. This finding is in agreement with [28]. The instability for $v_0^x < v_1^x \lesssim 2v_0^x$ is caused by an undesired rotation of the spot induced by numerical truncation errors. These accumulate during the simulation and eventually result in an asymmetric perturbation (with respect to y) acting on the spot pattern. Once the spot starts to rotate and eventually drifts away from the centerline $y = 0$, the proposed open-loop control $\mathbf{f}_{\text{Gold}}$ can neither respond nor correct the undesired rotation. The impact of the numerical truncation error becomes more pronounced with growing protocol's duration T_x and results in a broad unstable region for long protocols, $T_x > 10\, t_{\text{drift}}$.

The situation changes if one aims to move the spot pattern perpendicular to its intrinsic direction of propagation, here in y-direction. In Figure 4c, we keep the motion in x unchanged, $\Phi_x(t) = v_0^x\, t$, and accelerate the spot according to (4.3) along the y-direction. Because the controlled spot solution is symmetric with respect to the centerline $y = 0$, position control in y might be inherently unstable [28]. One notices immediately that regions with unstable position control are much larger compared to Figure 4a. Nevertheless, the control is stable for weak acceleration, $v_1^y \simeq 0.1 v_0^x$, independent of the protocol's duration. Increasing the terminal velocity further, Goldstone mode control starts to fail. Once a certain deviation between the current spots' position and the proposed POM is attained, the pattern cannot follow the applied control anymore and starts to move freely. With further growing terminal velocity v_1^y, the control's magnitude increases as well and thus successful position control can be re-stabilized. Longer protocols T_y result in an accumulating of numerical truncation errors.

4.1.2. Orientation control with speed adjustment

In the previous paragraph, we have demonstrated that the stability of position control can be enhanced if in any current position of the spot its symmetry axis, given by $\Phi_\varphi(t)$, points tangentially to the direction of motion. Therefore, in our next example, we propose to shift the spot pattern along a circular trajectory by simultaneously controlling its orientation

$$\Phi_x(t) = r \sin\left(\Phi_\varphi(t)\right), \quad \Phi_y(t) = -r\cos\left(\Phi_\varphi(t)\right), \quad \Phi_\varphi(t) = 2\pi t/T. \tag{4.4}$$

Here, r denotes the radius of the circle and T the protocol's duration. For experimental realization compare [41], for example.

In Figure 5, we present the temporal evolution of the activator distribution u (a) controlled by $\mathbf{f}_{\mathrm{Gold}}$ (b). In line with the POM, the spot always keeps its symmetry axis at the tangent to the desired trajectory of motion. The control $\mathbf{f}_{\mathrm{Gold}}$ remains localized and is dominated by the translational Goldstone mode $\partial_{\xi_x}\mathbf{U}_c$ due to the acceleration along $\boldsymbol{\Xi}(t)$ (4.4); the average speed is $\bar{v} \simeq 2.4 v_0^x$. Notably, the maximum value of the control magnitude is half as strong compared to position control without adjusting the orientation, $\Phi_\varphi(t) = 0$ (not explicitly shown). In panel (c), the temporal behavior of the relative error $\|f_{u,\mathrm{Gold}}(t) - f_{u,\mathrm{opt}}(t)\|_{L^1(\Omega)}/\|f_{u,\mathrm{Gold}}(t)\|_{L^1(\Omega)}$ measured by the $L^1(\Omega)$ norm is shown (solid line). They are large compared to pure position control along a Lissajous curve, *cf.* Figure 3. Stronger deviations are caused by interpolation errors arising during numerical rotation of spot patterns by $\Phi_\varphi(t)$. The relative error attains a maximum at $\Phi_\varphi(t) = m\,45°$, m odd. At these angles, the distance between the nodes of the rotated grid and the underlying one is the largest, viz., $dx/\sqrt{2}$, and, hence, numerical interpolation errors become significant. Contrarily, the relative error minimizes at $\Phi_\varphi(t) = m\,90°$, $m \in \mathbb{Z}$, at which both grids coincide. Remarkably, the normalized error $\|u_{\mathrm{Gold}}(t) - u_{\mathrm{opt}}(t)\|_{L^1(\Omega)}/\|u_{\mathrm{Gold}}(t)\|_{L^1(\Omega)}$ (dashed line), is still less than 10^{-3} at any instants of time despite that the deviation of the associated controls rises up to $\sim 25\%$.

4.2. Orientation control

If the uncontrolled spot propagates at non-zero velocity $\mathbf{v}_0 \neq \mathbf{0}$, the simplest way to navigate it through a spatial domain is to control exclusively its current orientation $\Phi_\varphi(t)$. If so, the translational components of the POM $\boldsymbol{\Xi}(t)$ are determined by

$$\dot{\Phi}_x(t) = v_0^x \cos\left(\Phi_\varphi(t)\right), \quad \dot{\Phi}_y(t) = v_0^x \sin\left(\Phi_\varphi(t)\right). \tag{4.5}$$

Clearly, one loses the possibility to control separately the x- and y-position of the pattern by limiting the speed to $\|\dot{\boldsymbol{\Phi}}(t)\| = v_0^x$. Inserting (4.5) into (3.6), the translational Goldstone modes drop out and we obtain

$$\mathbf{f}_{\mathrm{Gold}}(\mathbf{r}, t) = -\dot{\Phi}_\varphi(t)\partial_\varphi \mathbf{U}_c(\mathbb{A}(-\Phi_\varphi(t))\,(\mathbf{r} - \boldsymbol{\Phi}(t))). \tag{4.6}$$

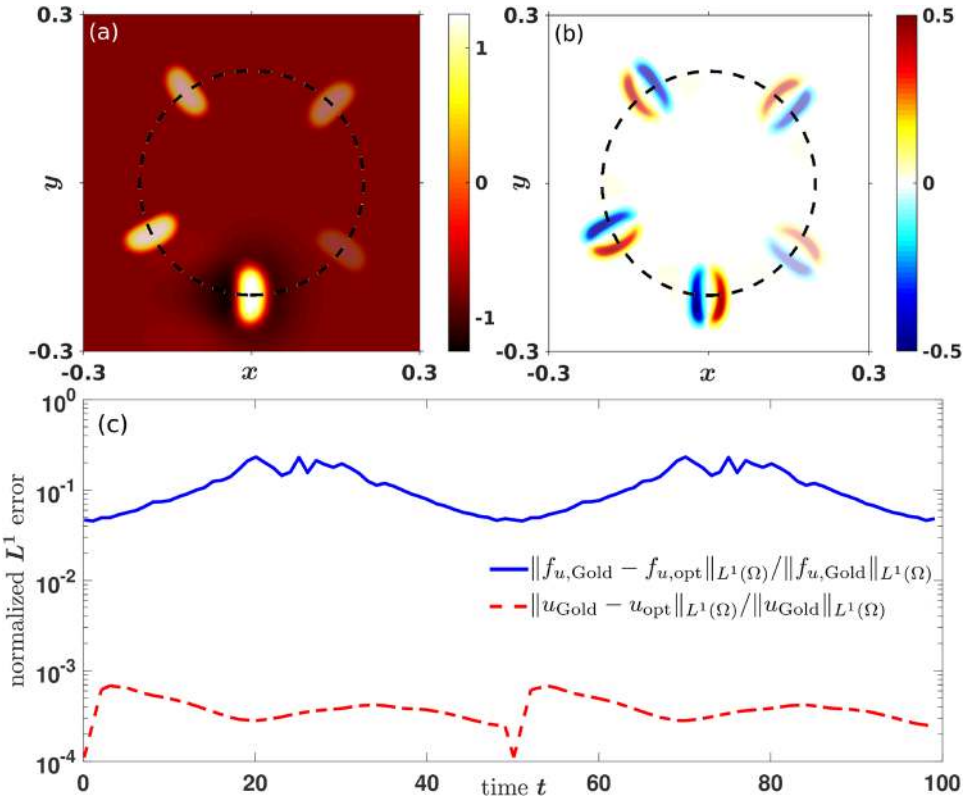

FIGURE 5. Position control along a circular desired distribution (4.4) with radius $r = 0.2$ and duration time $T = 200$; *cf.* [SI_video4]. (a) Snapshots of the activator distribution $u(\mathbf{r}, t)$ at time moments $t = \{30, 75, 120, 165, 200\}$. (b) Control $f_{u,\mathrm{Gold}}(\mathbf{r}, t)$ at the same instants of time. In (a) and (b), the dark dashed line indicates the POM and the decreasing transparency marks consecutive moments. (c) Temporal behavior of the relative $L^1(\Omega)$ error (4.2) between expression (3.2), $f_{u,\mathrm{Gold}}$ (3.6), and optimal activator control signals $f_{u,\mathrm{opt}}$ (3.8) during $t \in [0, T/2]$. We select set 1 in Table 1 for the kinetic parameters to (2.1) and set Tikhonov parameter to $\nu = 10^{-7}$.

Now, we pick up the problem formulated in Section 2, namely, how to prevent pinning of a spot at a local heterogeneity in the domain. The heterogeneity is viewed as circular region where the parameter κ_1 jumps from a background value κ_1^{back}, $\forall \mathbf{r} \notin \Omega_\circ$ to a defect value κ_1^{het}, $\forall \mathbf{r} \in \Omega_\circ$ whereby $\Omega_\circ = \{(x, y) \in \mathbb{R}^2 : (x+R)^2 + y^2 < R^2\}$ with radius $R = 0.05$. The orientational POM for avoiding the heterogeneity is set to

$$\Phi_\varphi(t) = \frac{\pi}{4} \sin\left(\frac{2\pi t}{T}\right), \tag{4.7}$$

with duration $T = L_x/v_0^x$. Note that the corresponding prescribed positions $(\Phi_x(t), \Phi_y(t))^T$ have to be calculated numerically.

In Figure 6, we present the temporal evolution of the activator distribution u in panel (a) and the corresponding control signal $f_{u,\mathrm{Gold}}$ in panel (b). The prescribed translational POM is indicated by the dashed lines. At first glance, the control signal possesses a more complicated shape and its magnitude is significantly reduced, $|f_{u,\mathrm{Gold}}| \lesssim 10^{-3}$, as compared to $|f_{u,\mathrm{Gold}}| \lesssim 10^{0}$ and $|f_{u,\mathrm{Gold}}| \lesssim 10^{-1}$ in the previous examples, *cf.* Figure 3 and Figure 5. Thus, orientation control is less invasive than position control. In return, we lose the ability for

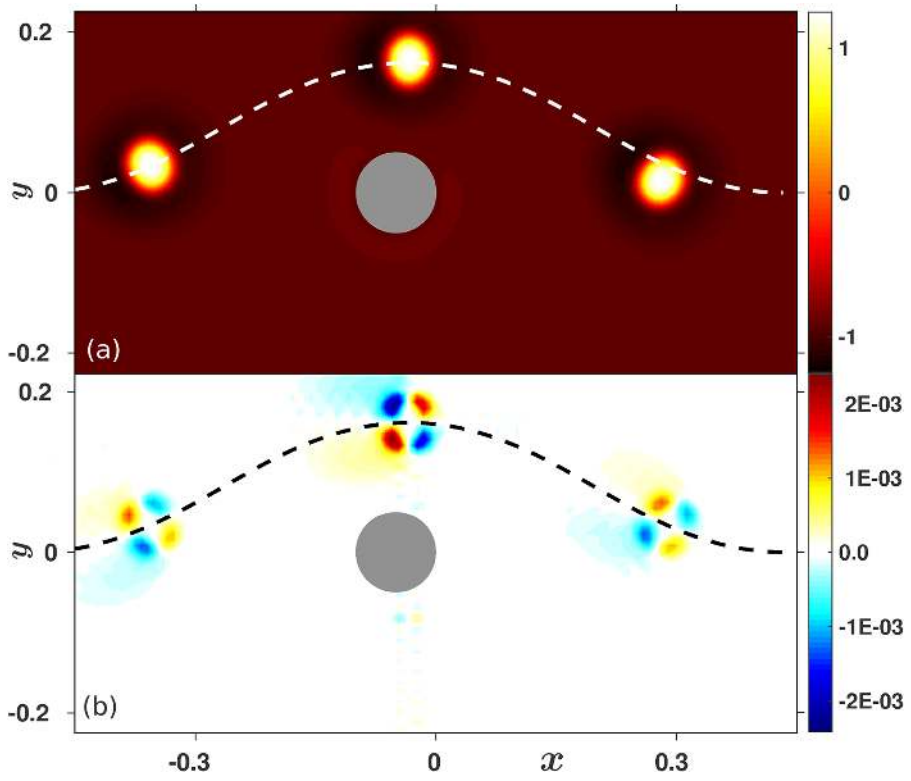

FIGURE 6. Orientation control to avoid collision with circular heterogeneity [SI_video5]. Snapshots of the activator u (a) controlled by $\mathbf{f}_{\text{Gold}}$ (b), (4.6), at different instants of time $t = \{100, 250, 400\}$. The controlled spot dynamics is simulated on a $(-0.5, 0.5] \times (-0.25, 0.25]$ domain with periodic boundary conditions using ETD2. We use the parameter set 2 in Table 1. The circular defect with radius $R = 0.05$ is modeled by a jump in κ_1 from its background value of $\kappa_1^{\text{back}} = -7.30$ to the value inside the heterogeneity $\kappa_1^{\text{het}} = -7.50$.

fast intervention into spot dynamics as well as for mayor increase in the speed of the spot. Additionally, orientation control is much more susceptible to fail. The small control magnitudes are too weak to suppress the impact of numerical round-off errors which may result in undesired spot rotation, *cf.* Section 4.1.1. Caused by the small propagation velocity, the duration T of the POM grows as compared to position control, see Section 4.1, and therefore the probability of failure increases as well.

4.3. Position control by a single control signal

So far, we have discussed examples of fully actuated systems for which the number of state components equals the number of independent control signals. If the coupling matrix $\mathbb{B}$ is not invertible, expression (3.6) for $\mathbf{f}_{\text{Gold}}$ cannot be used. The question arises how to extend our approach to underactuated systems [26, 31]. In the following example we assume a control acting on the activator u only while inhibitors v and w remain uncontrolled, *i.e.*, $f_{v,\text{Gold}}(\mathbf{r}, t) = f_{w,\text{Gold}}(\mathbf{r}, t) = 0$. Control via an inhibitor has been discussed in detail for the Hodgkin-Huxley model and the three-component Oregonator model for photosensitive BZ reaction, compare supplemental information to [26].

To derive an expression for $f_{u,\text{Gold}}(\mathbf{r}, t)$, we start with the fully actuated system

$$\partial_t u(\mathbf{r}, t) = D_u \Delta u + \kappa_2\, u - u^3 - \kappa_3 v - \kappa_4 w + \kappa_1 + f_u, \tag{4.8a}$$

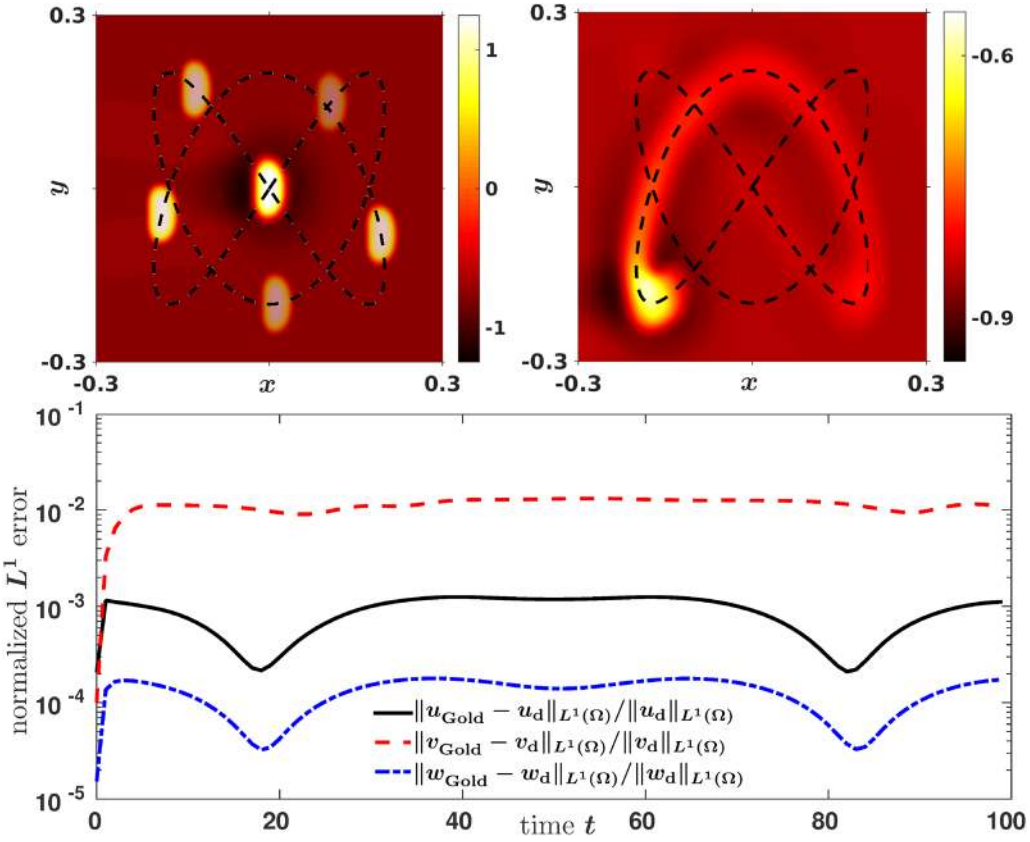

FIGURE 7. Position control by a single control signal acting on u, $\mathbf{f}_{\mathrm{Gold}} = (f_{u,\mathrm{Gold}}, 0, 0)^T$, along the Lissajous curve (4.1), see [SI_video6]. *Top left*: Time evolution of activator distribution u at time moments $t = \{10, 50, 90, 130, 170, 200\}$. The decreasing transparency marks consecutive instants of time. *Top right*: Distribution of the inhibitor v at $t = 180$. *Bottom*: Temporal behavior of the relative error as measured by the $L^1(\Omega)$ norm (4.2), between the numerically obtained states $\mathbf{U}$ and the desired distribution $\mathbf{U}_d$ during $t \in [0, T/2]$. We use parameter set 1 in Table 1 for the calculations.

$$\tau \partial_t v(\mathbf{r}, t) = D_v \Delta v + u - v + f_v, \tag{4.8b}$$
$$\theta \partial_t w(\mathbf{r}, t) = D_w \Delta w + u - w + f_w. \tag{4.8c}$$

Equations (4.8b)–(4.8c) are linear, inhomogeneous PDEs with initial conditions $v(\mathbf{r}, t_0) = v_0(\mathbf{r})$ and $w(\mathbf{r}, t_0) = w_0(\mathbf{r})$, respectively. Their solutions can be written as

$$\tilde{v}(\mathbf{r}, t) = \mathcal{K}_v^0 \circ v_0 + \frac{1}{\tau} \mathcal{K}_v \circ (u + f_v), \quad \tilde{w}(\mathbf{r}, t) = \mathcal{K}_w^0 \circ w_0 + \frac{1}{\theta} \mathcal{K}_w \circ (u + f_w), \tag{4.9}$$

where $\mathcal{K}_i^0$ and $\mathcal{K}_i$, $i \in \{v, w\}$, are integral operators involving Green's functions to the homogeneous equations corresponding to (4.8b)–(4.8c) with associated initial conditions and to the inhomogeneous equations with zero initial conditions. Plugging (4.9) into (4.8a) gives

$$\partial_t u(\mathbf{r}, t) = D_u \Delta u + \kappa_2\, u - u^3 - \kappa_3 \left[\mathcal{K}_v^0 \circ v_0 + \frac{1}{\tau} \mathcal{K}_v \circ u \right] - \kappa_4 \left[\mathcal{K}_w^0 \circ w_0 + \frac{1}{\theta} \mathcal{K}_w \circ u \right] + \kappa_1$$

$$+ f_u - \frac{\kappa_3}{\tau}\mathcal{K}_v \circ f_v - \frac{\kappa_4}{\theta}\mathcal{K}_w \circ f_w. \tag{4.10}$$

From the last line of (4.10) we identify the expression for $f_{u,\mathrm{Gold}}(\mathbf{r},t)$ to be

$$\tilde{f}_{u,\mathrm{Gold}}(\mathbf{r},t) = f_{u,\mathrm{Gold}}\,(\mathbf{r},\mathbf{t}) - \frac{\kappa_3}{\tau}\mathcal{K}_v \circ f_{v,\mathrm{Gold}} - \frac{\kappa_4}{\theta}\mathcal{K}_w \circ f_{w,\mathrm{Gold}}, \tag{4.11}$$

whereby the component of $\mathbf{f}_{\mathrm{Gold}}$ are determined by (3.6).

As an example for position control by a single control signal, we guide a spot along the Lissajous curve given by (4.1) with radius $r = 0.2$ and protocol duration $T = 200$. The spot's orientation $\Phi_\varphi(t) = 0$ remains uncontrolled. The relative errors between desired and controlled states are shown in Figure 7 (bottom). All states are obtained from numerical simulation of (2.1)–(3.1a) with control $\mathbf{f}_{\mathrm{Gold}} = (f_{u,\mathrm{Gold}}, 0, 0)^T$ given by (4.11). The relative error for the activator u (solid line) is less than 10^{-3} at any time t and thus the controlled activator pattern agrees satisfactorily well with the desired distribution. This finding is corroborated by snapshots of u at different instants of time in Figure 7 (top left). In contrast to the activator, the profile of the inhibitor v is not preserved under control but deformed considerably, see Figure 7 (top right). In particular, an elongated region of activity becomes apparent along the Lissajous curve due to time scale separation in the RDS (2.1). The concentration of the slow inhibitor v, produced in the wake of the activator, decays exponentially to the rest state on a time scale $\tau = 48 \approx T/4$. Consequently, the relative error of v (dashed line) attains relatively large values of the order 10^{-2}. On the other hand, the fast inhibitor w and the activator u vary on the same characteristic time scale as $\theta = 1$ was chosen in the considered example. Thus, we expect only small changes in both profiles in the presence of the control. In fact, the values of the relative error for w turn out to be less than 10^{-4} which is even one magnitude smaller than the relative error of u, *cf.* the dash-dotted line in Figure 7 (bottom).

5. Conclusion

Localized traveling chemical, chemo-mechanical, electrical or neural activity is ubiquitous in spatially extended nonlinear systems driven far from thermodynamic equilibrium. Hence, to control the current position, orientation and velocity of a traveling spot is a key challenge not only under general aspects but particularly from the perspective of numerous applications. We have demonstrated that the control signals, which one has to apply to solve these tasks, can be analytically expressed by the Goldstone modes of the uncontrolled spot. The control acts locally as long as the Goldstone modes are localized, and preserves the spatial profile of the spot as long as the spectral gap between deformation modes and Goldstone modes in the linear stability operator of the uncontrolled spot solution is sufficiently large.

We would like to stress that a complete knowledge about the underlying nonlinear kinetics $\mathbf{R}(\mathbf{U})$ responsible for the spontaneous formation of the spot is not required in order to determine the control $\mathbf{f}_{\mathrm{Gold}}$ for a given protocol of motion. According to (3.6), we can express the control amplitude through the derivative of the uncontrolled spot profile $\mathbf{U}_c$, *i.e.*, $\mathbf{R}(\mathbf{U})$ does not enter explicitly into the expression for $\mathbf{f}_{\mathrm{Gold}}$. Thus, if $\mathbf{R}(\mathbf{U})$ is known, as in case of the RD model (2.1), we numerically solve the nonlinear eigenvalue problem (3.3) and calculate $\mathbf{f}_{\mathrm{Gold}}$ from (3.6). However, often in practical applications the complete scheme of kinetic steps specifying $\mathbf{R}(\mathbf{U})$ is known only approximately because some kinetic steps are unclear or hidden. Nevertheless, if in those cases the stationary profile and the propagation velocity of the uncontrolled spot can be measured with sufficient accuracy, then the method works. In our view, this aspect might extend the applicability of Goldstone mode control considerably.

Strictly speaking, localized spots are solutions on an infinite spatial domain. Our results are correct as long as the spot weakly interacts with the domain boundaries. This will be the case if the domain size is much larger than the characteristic diameter of the spot, l. When we compare the analytical results with numerical simulations, we use periodic boundary conditions with spatial periods much larger than l. The interaction range of a spot with a Neumann boundary is determined by the so-called response functions. These are the eigenfunctions of

the adjoint linear stability operator of the uncontrolled spot. Usually, they are well localized and, therefore, the effective interaction between spots or between a spot and a Neumann boundary is short-ranged.

Goldstone mode control is realized by external spatio-temporal forcing, *i.e.*, it is an open-loop control. Contrary to closed-loop or feedback control, continuous monitoring of the system is not required. On the downside, as any open-loop control, the method is sensitive to perturbations. Therefore, the range of applicability has been checked by a stability analysis.

Based on general symmetry considerations, Goldstone mode control is widely applicable. So far, the method has been successfully used to guide traveling interfaces and excitation pulses in 1D [26, 42] and spiral waves [42] as well as to shape iso-concentration lines of traveling wave patterns [29] in 2D. Recently, we successfully applied Goldstone mode control to spot solutions of neural field equations [56] that phenomenologically describe the dynamics of synaptically coupled neurons [11]. Remarkably, in all examples considered so far, Goldstone mode control is, within numerical accuracy, equal to solutions of an equivalent, non-regularized optimal control problem. Consequently, our control turns out to be optimal, *i.e.*, no other control enforces the system closer to the desired target state according to the protocol of motion. Furthermore, these control signals have been proven to be excellent initial conditions for regularized optimal control problems achieving a substantial computational speed-up. Generally, Goldstone mode control might serve as consistency check for numerical optimal control algorithms as well.

We emphasize that optimal control is not only computationally demanding but requires full knowledge of the nonlinear kinetics. On the other hand, the scope of optimal control can be extended in various ways: More general objective functionals than stated above can be studied, *cf.* [21]. Optimal control can also easily deal with control signals confined to prescribed spatial regions or with upper and lower bounds for the control amplitudes in the form of inequalities, *i.e.*, $-\infty < f_a \leq f_i(\mathbf{r},t) \leq f_b < \infty$, $\forall i = 1,\dots,n$. Moreover, by adding a multiple of the L_1-norm of the control to the objective functional J, sparse optimal controls are obtained. Sparsity means that the optimal control vanishes in certain regions. The level of sparsity depends on a so-called sparsity parameter. The larger this parameter is the larger is the region where the optimal control is exactly zero. In this way, the optimal control is concentrated on regions that are most important for the minimization. However, this is a more intuitive interpretation of sparsity that cannot be exactly quantified. For technical details as well as examples, we refer to [7–9, 21, 42].

Appendix A. Details on numerical methods

In our numerical simulations, the state equation

$$\partial_t \mathbf{U}(\mathbf{r},t) - \mathbb{D}\Delta\mathbf{U}(\mathbf{r},t) - \mathbf{R}(\mathbf{U}(\mathbf{r},t)) = \mathbf{f}(\mathbf{r},t), \tag{A.1a}$$

is solved on a rectangular domain $\Omega = (x_a, x_b] \times (y_a, y_b]$ with periodic boundary conditions

$$\begin{aligned} \mathbf{U}(x_a,y,t) &= \mathbf{U}(x_b,y,t), & \frac{\partial}{\partial x}\mathbf{U}(x_a,y,t) &= \frac{\partial}{\partial x}\mathbf{U}(x_b,y,t), \\ \mathbf{U}(x,y_a,t) &= \mathbf{U}(x,y_b,t), & \frac{\partial}{\partial y}\mathbf{U}(x,y_a,t) &= \frac{\partial}{\partial y}\mathbf{U}(x,y_b,t). \end{aligned} \tag{A.1b}$$

Here, $\mathbf{U}(\mathbf{r},t) = (u_1(\mathbf{r},t),\dots,u_n(\mathbf{r},t))^T$ is the vector of $n \in \mathbb{N}$ state components defined in the two-dimensional spatial domain $\Omega \subset \mathbb{R}^2$ with $\mathbf{r} = (x,y)^T$. Further, $\mathbf{R}(\mathbf{U}) = (R_1(\mathbf{U}),\dots,R_n(\mathbf{U}))^T$ describes the nonlinear kinetics of the components and the $n \times n$ matrix $\mathbb{D}$ of constant diffusion coefficients is assumed to be diagonal $\mathbb{D} = \mathrm{diag}(D_1,\dots,D_n)$ (isotropic medium). On the right hand side of (A.1a), the space-time dependent control signals are denoted by $\mathbf{f}(\mathbf{r},t) = (f_1(\mathbf{r},t),\dots,f_m(\mathbf{r},t))^T$, $m \in \mathbb{N}$.

Without loss of generality, we fix the spot's direction of motion to coincide with the x-axis, *i.e.*, $v_0^x \neq 0$ and $v_0^y = 0$. Any numerical simulation to equation (A.1a) are initialized with the profile $\mathbf{U}_c$. The latter and the

natural velocity $\mathbf{v}_0$ are obtained by solving the nonlinear eigenvalue problem

$$\mathbf{0} = \mathbb{D}\Delta_{\boldsymbol{\xi}}\mathbf{U}_c(\boldsymbol{\xi}) + \mathbf{v}_0 \cdot \nabla_{\boldsymbol{\xi}}\mathbf{U}_c(\boldsymbol{\xi}) + \mathbf{R}(\mathbf{U}_c(\boldsymbol{\xi})), \tag{A.2}$$

with adequate accuracy.

A.1 Simulations based on the Goldstone mode control $\mathbf{f}_{\mathbf{Gold}}$

In all position control examples based on Goldstone mode control, we numerically solve (A.1) with spectral methods [12]. Transforming (A.1a) into the Fourier space, one gets for the n-th state component

$$\frac{\partial}{\partial t}\hat{u}_n(\mathbf{k},t) = -D_n\,\mathbf{k}^2\,\hat{u}_n(\mathbf{k},t) + \mathcal{F}\{R_n(\mathbf{U}) + f_n(\mathbf{U},t)\}, \tag{A.3}$$

where $\hat{u}_n$ denotes the Fourier transform $\mathcal{F}\{\cdot\}$ of the n-th component, $\hat{u}_n(\mathbf{k},t) = \mathcal{F}\{u_n(\mathbf{r},t)\}$, and $\mathbf{k} = (k_x, k_y)^T$ is the wave vector. Multiplying (A.3) by $\mathrm{e}^{-c_n t}$ with $c_n = D_n\mathbf{k}^2$ and integrating the equation over a single time step from t_m to $t_{m+1} = t_m + \mathrm{d}t$, one derives the exponential time differencing (ETD) method

$$\begin{aligned}\hat{u}_n(\mathbf{k},t_{m+1}) = {}& \hat{u}_n(\mathbf{k},t_m)\mathrm{e}^{c_n\mathrm{d}t} \\ &+ \mathrm{e}^{c_n\mathrm{d}t}\int_0^{\mathrm{d}t}\mathrm{d}\tau\,\mathrm{e}^{-c_n\tau}\mathcal{F}\{R_n(\mathbf{U}(t_m+\tau),t_m+\tau) + f_n(\mathbf{U}(t_m+\tau),t_m+\tau)\}.\end{aligned} \tag{A.4}$$

This formula is exact. The essence of ETD methods is in approximating the integral in this expression. We use ETD2 implying that

$$\mathcal{F}\{g(\mathbf{U}(t_m+\tau),t_m+\tau)\} = \mathcal{F}\{g(\mathbf{U}(t_m),t_m)\} + \tau\left(\mathcal{F}\{g(\mathbf{U}(t_m),t_m)\} - \mathcal{F}\{g(\mathbf{U}(t_{n-1}),t_{n-1})\}\right)/\mathrm{d}t + \mathcal{O}(\mathrm{d}t^2).$$

Finally, one arrives at the numerical scheme for ETD2

$$\begin{aligned}\hat{u}_n(\mathbf{k},t_{m+1}) = {}& \hat{u}_n(\mathbf{k},t_m)\mathrm{e}^{c_n\mathrm{d}t} \\ &+\mathcal{F}\{R_n(\mathbf{U}(t_m),t_m) + f_n(\mathbf{U}(t_m),t_m))\}\frac{\left((1+c_n\,\mathrm{d}t)\mathrm{e}^{c_n\mathrm{d}t} - 2\,c_n\,\mathrm{d}t - 1\right)}{c_n^2\,\mathrm{d}t} \\ &+\mathcal{F}\{R_n(\mathbf{U}(t_{m-1}),t_{m-1}) + f_n(\mathbf{U}(t_{m-1}),t_{m-1}))\}\frac{\left(1+c_n\,\mathrm{d}t - \mathrm{e}^{c_n\mathrm{d}t}\right)}{c_n^2\,\mathrm{d}t},\end{aligned} \tag{A.5}$$

which has a local truncation error of $\mathcal{O}(5\,\mathrm{d}t^3\,\ddot{\mathcal{F}}\{\cdot\}/12)$ [12]. To avoid interpolation errors due to discretization of the spatial domain, both the desired solution $\mathbf{U}_d(\mathbf{r},t) = \mathbf{U}_c(\mathbb{A}(-\Phi_\varphi(t))\,(\mathbf{r} - \boldsymbol{\Phi}(t)))$ and $\mathbf{f}_{\mathrm{Gold}}$

$$\mathbf{f}_{\mathrm{Gold}}(\mathbf{r},t) = \left[\left(\begin{pmatrix}v_0^x\\v_0^y\\0\end{pmatrix} - \mathbb{A}_z\left(-\Phi_\varphi(t)\right)\begin{pmatrix}\dot{\Phi}_x(t)\\\dot{\Phi}_y(t)\\\dot{\Phi}_\varphi(t)\end{pmatrix}\right)\cdot\tilde{\nabla}_{\boldsymbol{\xi}}\right]\mathbf{U}_c(\boldsymbol{\xi})\Big|_{\boldsymbol{\xi}=\mathbb{A}(-\Phi_\varphi(t))(\mathbf{r}-\boldsymbol{\Phi}(t))}, \tag{A.6}$$

are computed with spectral methods[1]. First, the uncontrolled spot profile $\mathbf{U}_c(\mathbf{r})$ is rotated around $(0,0)^T$ in the spatial domain by $\Phi_\varphi(t)$, see Figure A.1(b). In a second step, the shift as given by the translational POM

[1] $\mathbb{A}(\alpha) = [\cos(\alpha), -\sin(\alpha); \sin(\alpha), \cos(\alpha)]$ denotes the clockwise rotation matrix in 2D and $\mathbb{A}_z(\alpha)$ is the clockwise rotation matrix around the z-axes in 3D, $\mathbb{A}_z(\alpha) = \mathrm{diag}(\mathbb{A}(\alpha), 1)$.

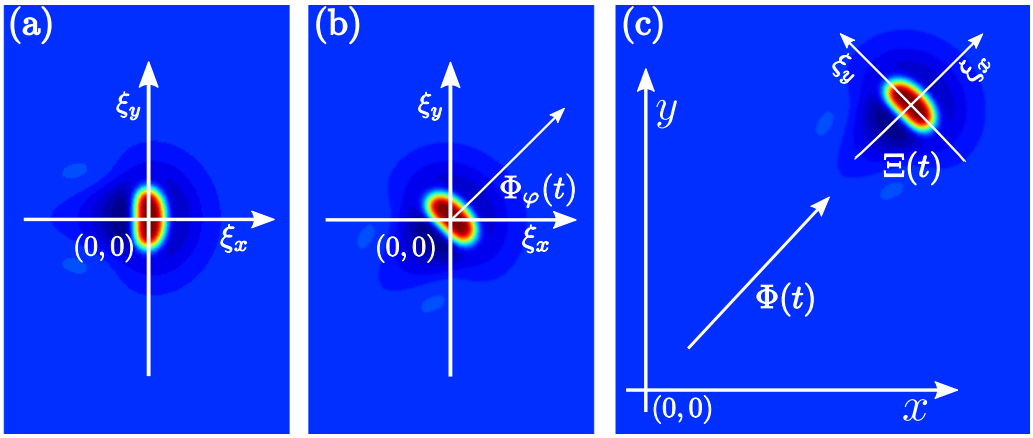

FIGURE A.1. Position and orientation of the desired distribution $\mathbf{U}_d(\mathbf{r},t) = \mathbf{U}_c(\mathbb{A}(-\Phi_\varphi(t))(\mathbf{r}-\mathbf{\Phi}(t)))$. (a) Wave profile of the activator distribution $u_c(\boldsymbol{\xi})$ centered in the co-moving and co-rotating frame of reference at $\boldsymbol{\xi} = (0,0)^T$. (b) Counter-clockwise rotation of $u_c(\boldsymbol{\xi})$ according to the desired orientation $\Phi_\varphi(t)$. (c) Shift of the rotated solution in virtue of the translational protocol of motion $\mathbf{\Phi}(t) = (\Phi_x(t), \Phi_y(t))^T$.

$\mathbf{\Phi}(t) = (\Phi_x(t), \Phi_y(t))^T$, cf. Figure A.1(c), is computed in Fourier space by multiplying the Fourier transform of the previously rotated spot solution with $\exp(-i\mathbf{k}\cdot\mathbf{\Phi}(t))$, followed by the inverse Fourier transform $\mathcal{F}^{-1}\{\cdot\}$.

Analogously, we calculate $\mathbf{f}_{\text{Gold}}$: First, the derivatives with respect to x and y are obtained numerically in Fourier space using $\partial_x\mathbf{U}_c = \mathcal{F}^{-1}\{ik_x\mathcal{F}\{\mathbf{U}_c\}\}$ and $\partial_y\mathbf{U}_c = \mathcal{F}^{-1}\{ik_y\mathcal{F}\{\mathbf{U}_c\}\}$, respectively. The angular derivative is given as the linear combination $\partial_\varphi\mathbf{U}_c = -y\partial_x\mathbf{U}_c + x\partial_y\mathbf{U}_c$. Second, all derivatives are rotated according to the orientational POM $\Phi_\varphi(t)$, followed by a shift computed in Fourier space.

In all simulations using ETD2, the squared domain $\Omega = (-0.5, 0.5] \times (-0.5, 0.5]$ is discretized into 256×256 spatial grid points and Fourier modes, respectively. We emphasize that the domain size is chosen sufficiently large to avoid self-interaction of the spots in the periodic simulation domain. The numerical time step $\mathrm{d}t$ is adjusted such that the local truncation error is less than 10^{-4} for any protocol of motion. But $\mathrm{d}t$ is always less or equal to 0.01.

A.2 Numerical calculation of optimal control

For optimal control, both the state equation (A.1) and the adjoint equation

$$-\partial_t\mathbf{P}(\mathbf{r},t) - \mathbb{D}\Delta\mathbf{P}(\mathbf{r},t) - \mathcal{D}\mathbf{R}^T(\mathbf{U}(\mathbf{r},t))\mathbf{P}(\mathbf{r},t) = \mathbf{U}-\mathbf{U}_d \quad \text{in} \quad Q, \tag{A.7}$$

have to be solved for any iterate $\mathbf{f}$. In (A.7) $\mathbf{U}$ is the state associated to $\mathbf{f}$. It has to be computed prior to solving (A.7). The *adjoint state* $\mathbf{P}$ has to obey the terminal condition $\mathbf{P}(\cdot,T) = \mathbf{0}$ in Ω at final time T and periodic boundary conditions in $\partial\Omega$. In equation (A.7), $\mathcal{D}\mathbf{R}^T$ denotes the transposed Jacobian matrix of $\mathbf{R}$ with respect to $\mathbf{U}$. The solution to the optimal control problem is determined by solving the system

$$\mathbf{P} + \nu\,\mathbf{f}_{\text{opt}} = \mathbf{0} \tag{A.8}$$

for $\mathbf{f}$. Due to the mixed initial and terminal conditions for $\mathbf{U}$ and $\mathbf{P}$ it is rarely possible to find numerical solutions to optimal control by a direct integration method. To reduce numerical costs, we employ Model Predictive Control and divide our optimal control problem into subproblems with a 4 time-step small time-horizon [42]. Thereby, each subproblem is solved with a gradient-type method which proceeds as follows: Starting for $k = 1$

with an initial guess $\mathbf{f}_{k-1} \equiv \mathbf{f}_0$ for the control, we compute $\mathbf{U}_k$ as the solution to (A.1) as well as $\mathbf{P}_k$ as the solution to (A.7) with $\mathbf{U}_k$ substituted for $\mathbf{U}$. The gradient of the non-negative tracking-type functional J with respect to $\mathbf{f}$, $\mathbf{d}_k$, is calculated as $\mathbf{d}_k = \mathbf{P}_k + \nu\,\mathbf{f}_{k-1}$ whereby $-\mathbf{d}_k$ defines the direction of steepest descent in function space. A new control $\mathbf{f}_k$ is iteratively obtained by

$$\mathbf{f}_k := \mathbf{f}_{k-1} - s\,\mathbf{d}_k, \tag{A.9}$$

where s denotes a suitable step size [20, 21]. If $\mathbf{d}_k$ satisfies an appropriately chosen termination condition, in our work this is set to $\|\mathbf{d}_k\| < 10^{-8}$, then the algorithm stops and $\mathbf{f}_k$ is taken as $\mathbf{f}_{\text{opt}}$. Otherwise, the steps are repeated iteratively for $k := k + 1$. Because the convergence of a gradient-type method can be fairly slow, the maximum number of iterations has been limited to $N_{\text{iter}} = 50$. Moreover, we keep the Tikhonov-regularization parameter fixed at $\nu = 10^{-7}$.

Many modifications of the basic algorithm sketched above exist and often lead to a better performance, as, *e.g.*, the nonlinear conjugate gradient method [4]. However, all iterative algorithms require multiple solutions of state and adjoint state equation, resulting in a rapidly increasing computational cost of numerical optimal control with the number of spatial dimensions and the length of the time interval. Therefore, the domain Ω is discretized by 256 grid points in each direction with spatial step sizes of $dx = dy = 1/256$ and the Laplacian Δ is approximated by a 5-point stencil. Due to significant computational cost of the gradient-type algorithm, we choose a moderate temporal resolution of $\mathrm{d}t = 0.1$. For maximum stability the time evolution is computed with an implicit Euler method.

A.3 Error estimation

While the numerical evaluation of $\mathbf{f}_{\text{Gold}}$ is limited by the accuracy of the first spatial derivatives $\tilde{\nabla}_{\boldsymbol{\xi}}\mathbf{U}_c$, the numerical computations of $\mathbf{f}_{\text{opt}}$ is affected by errors arising both in the discretization of space and time. We stress that $\mathbf{f}_{\text{Gold}}$ is calculated using spectral differentiation, while we have to use finite difference stencils for the simulation of both the state (A.1) and adjoint equation (A.7) in order to reduce computational costs. Nevertheless, the limiting error arises from the time step chosen in the implicit Euler-scheme. Despite that the latter is A-stable, the local truncation error is $\mathcal{O}(\mathrm{d}t^2)$ and the error at a specific time t is of the order of $\mathcal{O}(\mathrm{d}t)$. Consequently, one can expect that the relative error $\|f_{u,\text{Gold}} - f_{u,\text{opt}}\|$ is in the L^2-norm bounded from above by $\mathcal{O}(\mathrm{d}t)$.

A.4 Simulation times

As already mentioned, optimal control algorithm requires much more computational resources compared to the analytic expression f_{Gold}. For instance, the computation of optimal position control along the Lissajous curve, see Figure 4, with a short period of $T = 200$, *i.e.*, 2000 time iterations steps with $\mathrm{d}t = 0.1$, takes roughly 50 hours by using 3 cores (Intel i5 − 6500 with 3.20GHz) in parallel. Contrary, the same numerical simulation of (A.1) based on $\mathbf{f}_{\text{Gold}}$ runs approximately one hour on the same PC. The relatively short simulation times enable us not only to use integration schemes with smaller numerical truncation error, *e.g.*, spectral methods with ETD2 [12], but also to move the spot along longer, more complex trajectories [SI_video2,SI_video3].

Appendix B. Traveling spot interacting with a circular heterogeneity of jump type

The interaction of traveling spots with different types of parameter heterogeneities in 1D and 2D has been studied in detail by many authors, see [36] and references therein. Penetration, rebound, annihilation, oscillation, as well as stationary or oscillatory pinning of spots were observed. Figure B.1 illustrates different outcomes of the interaction between a traveling spot and a localized circular defect formed by a finite jump $\delta k_1 = \kappa_1^{\text{het}} - \kappa_1^{\text{back}}$ from a background value κ_1^{back} and a higher value κ_1^{het} inside the circular heterogeneity. Additionally, other scenarios of spot-defect interaction have been found like repeated creation of spots inside the heterogeneity as

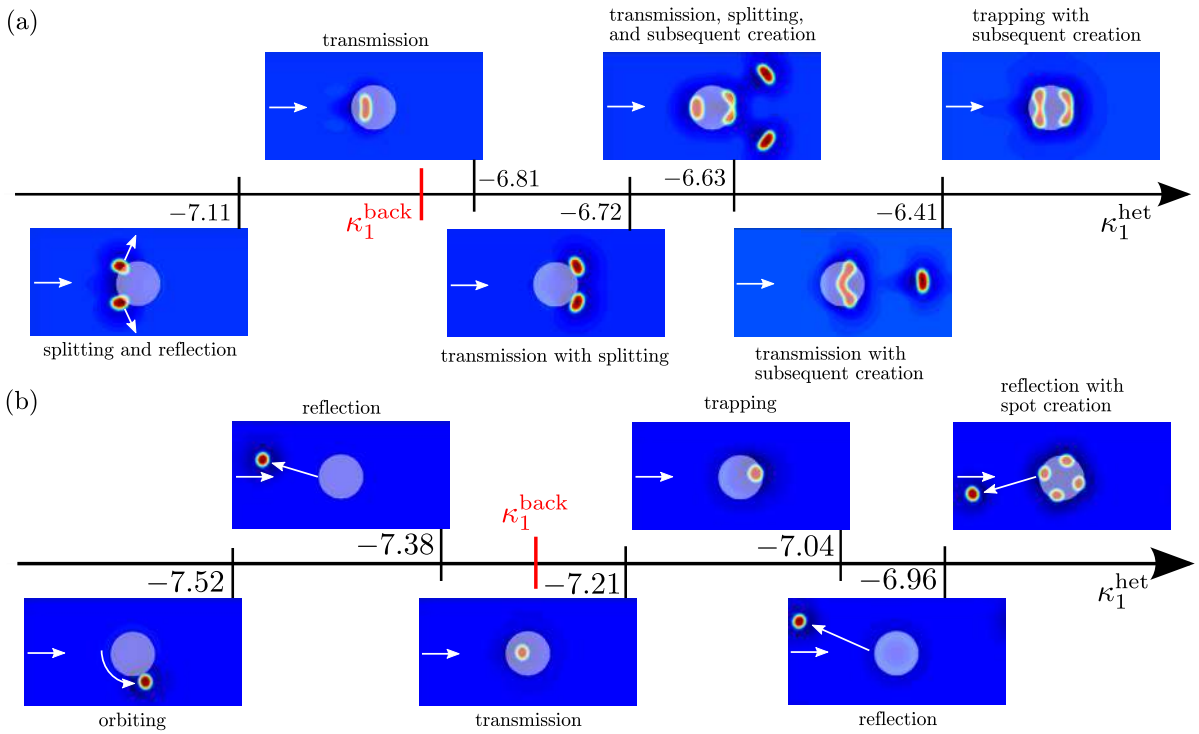

FIGURE B.1. Interaction of a traveling spot with a circular defect (light blue). (a) Splitting and different regimes of transmission or nucleation of new spots [SI_video1]. Parameter set 1 in Table 1 (main manuscript) with $\kappa_1^{back} = -6.92$. (b) Trapping, reflection, transmission, and nucleation of new spots. Parameter set 2 in Table 1 (main manuscript) with $\kappa_1^{back} = -7.30$: Shown are snapshots of the activator distribution in a rectangular spatial domain of size $\Omega = [0, 1) \times [-0.25, 0.25)$ with periodic boundary conditions. Simulations were performed using ETD2 in time, *cf.* Appendix A.

well as spots orbiting both inside and outside of the defect boundary. If the activator describes the temperature in a catalytic packed-bed reactor, resting *hot spots* [32] or those pinned to local heterogeneities can damage the catalyst support. In particular, collision of *hot spots* with the reactor walls must be prevented for safety reasons. Consequently, guidance of a traveling spot with given velocity along a desired trajectory through a bounded spatial domain might be a particular challenge in chemical engineering applications.

In the numerical simulations we realize a local heterogeneity in the medium by a circular defect of jump type (step-function) in the additive parameter κ_1:

$$\kappa_1(\mathbf{r}) = \begin{cases} \kappa_1^{\text{back}}, & \forall \mathbf{r} \notin \Omega_\circ, \\ \kappa_1^{\text{het}}, & \forall \mathbf{r} \in \Omega_\circ, \end{cases} \tag{B.1}$$

where the circular domain with radius R is centered at $(0, 0)$ and is defined by $\Omega_\circ = \{(x, y) \in \mathbb{R}^2 : x^2 + y^2 < R^2\}$. To start a numerical collision experiment, we initiate one spot moving rightwards ($v_0^x > 0$) at the far left edge of the simulation domain and measure the response to a circular defect with radius $R = 0.1$ located at $(0, 0)$.

The outcomes of collisions are classified in Figure B.1 depending on the difference ϵ between the constant background value κ_1^{back} and κ_1^{het} inside the heterogeneity, $\epsilon = \kappa_1^{\text{het}} - \kappa_1^{\text{back}}$. For the parameter set 1 in table 1 with $\kappa_1^{\text{back}} = -6.92$, one observes three qualitatively different regimes: splitting, transmission, and nucleation of new spots, Figure B.1(a). If κ_1^{het} is smaller than the background value, the single initiated spot splits into two

when reaching the left edge of the heterogeneity. Thereby, the initial velocity vector is conserved. Increasing the value of κ_1^{het} and thus decreasing the difference ϵ, the spot is able to pass the defect. With growing difference ϵ, spots first enter the defect and split into multiple solutions when leaving the obstacle at the right edge. Further increasing ϵ results in multiple creation of spots inside the defect. For $\kappa_1^{\text{het}} \gg \kappa_1^{\text{back}}$, the spot is able to enter the defect, gets trapped inside, and initiates the creation of multiple spots.

The observed scenarios of spot-defect-interactions are different for the second parameter set in table 2 and $\kappa_1^{\text{back}} = -7.30$. There, one discovers three qualitatively different regimes: trapping, transmission, and reflection, Figure B.1(b). For $\kappa_1^{\text{het}} \ll \kappa_1^{\text{back}}$, the spot pins at the outer edge of the defect and starts to move around the heterogeneity. With shrinking difference ϵ, the spot gets first reflected for $\kappa_1^{\text{het}} < \kappa_1^{\text{back}}$, then is able to pass the defect for $\epsilon \approx 0$, and eventually gets trapped inside the heterogeneity for $\epsilon \in [0.09, 0.26]$. In the last scenario, the trapped spot eventually performs circular motion at the inside of the defect. A further increase of κ_1^{het} results in various reflection scenarios.

Finally, we remark that parameter gradients and the geometrical shape of a heterogeneity will impact the interaction between traveling spots.

Appendix C. Asymptotic perturbation analysis – projection method

We presume that the uncontrolled reaction-diffusion system (A.1a) possesses a stable traveling wave (TW) solution $\mathbf{U}_c$ which either propagates smoothly with velocity $\mathbf{v}_0 = (v_0^x, v_0^y)^T$ or rotates around its center of rotation with angular velocity ω_0. Such a pattern satisfies

$$\mathbf{0} = \mathbb{D}\Delta_{\boldsymbol{\xi}}\mathbf{U}_c(\boldsymbol{\xi}) + \omega_0\partial_{\tilde{\varphi}}\mathbf{U}_c(\boldsymbol{\xi}) + (\mathbb{A}(-\omega_0 t)\mathbf{v}_0)\cdot\nabla_{\boldsymbol{\xi}}\mathbf{U}_c(\boldsymbol{\xi}) + \mathbf{R}(\mathbf{U}_c(\boldsymbol{\xi})), \tag{C.1}$$

in the frame of reference $\boldsymbol{\xi} \equiv (\xi_x, \xi_y)^T = \mathbb{A}(-\omega_0 t)(\mathbf{r} - \mathbf{v}_0 t)$ co-moving with the velocity $\mathbf{v}_0$ and co-rotating with angular frequency ω_0. Here, $\mathbb{A}(\alpha) = [\cos(\alpha), -\sin(\alpha); \sin(\alpha), \cos(\alpha)]$ is the clockwise rotation matrix in 2D. In the co-moving coordinates $\boldsymbol{\xi}$, the angular derivative is given by $\partial_{\tilde{\varphi}} = -\xi_y\partial_{\xi_x} + \xi_x\partial_{\xi_y}$. Obviously, (C.1) depends explicitly on time t if the TW pattern simultaneously moves and rotates, $\omega_0\mathbf{v}_0 \neq \mathbf{0}$. Consequently, we have to claim that the considered pattern either moves, solely rotates, or is at rest, *i.e.*, $|\mathbf{v}_0| = \omega_0 = 0$. In what follows, we keep both characteristic quantities in our derivations but always have in mind that at least one of them must be zero.

C.1 Goldstone modes and response functions

The stability of the TW pattern $\mathbf{U}_c$ is determined by the eigenvalues of the linear stability operator $\mathcal{L}$. The latter arises by expanding (C.1) around $\mathbf{U}_c$

$$\mathcal{L} = \mathbb{D}\Delta_{\boldsymbol{\xi}} + \omega_0\partial_{\tilde{\varphi}} + (\mathbb{A}(-\omega_0 t)\mathbf{v}_0)\cdot\nabla_{\boldsymbol{\xi}} + \mathcal{D}\mathbf{R}(\mathbf{U}_c(\boldsymbol{\xi})), \tag{C.2}$$

in the frame of reference $\boldsymbol{\xi}$. Thereby, $\mathcal{D}\mathbf{R}(\mathbf{U}_c)$ denotes the Jacobian matrix of $\mathbf{R}$ evaluated at $\mathbf{U}_c$. Since we presume that $\mathbf{U}_c(\boldsymbol{\xi})$ is stable, the eigenvalue of $\mathcal{L}$ with the largest real part is $\lambda_0 = 0$ and the corresponding eigenfunctions $\mathbf{W}_i(\boldsymbol{\xi})$, $i \in \{\xi_x, \xi_y, \tilde{\varphi}\}$, also called the *propagator modes*, can be expressed by the Goldstone modes $\partial_i\mathbf{U}_c(\boldsymbol{\xi})$, $i \in \{\xi_x, \xi_y, \tilde{\varphi}\}$. Calculating the derivative of (C.1) with respect to ξ_x, ξ_y, and $\tilde{\varphi}$, one gets

$$0 = \mathcal{L}\partial_{\xi_x}\mathbf{U}_c(\boldsymbol{\xi}) + \omega_0\,\partial_{\xi_y}\mathbf{U}_c(\boldsymbol{\xi}), \tag{C.3a}$$
$$0 = \mathcal{L}\partial_{\xi_y}\mathbf{U}_c(\boldsymbol{\xi}) - \omega_0\,\partial_{\xi_x}\mathbf{U}_c(\boldsymbol{\xi}), \tag{C.3b}$$
$$0 = \mathcal{L}\partial_{\tilde{\varphi}}\mathbf{U}_c(\boldsymbol{\xi}) - \mathbf{v}_0\times\nabla_{\boldsymbol{\xi}}\mathbf{U}_c(\boldsymbol{\xi}). \tag{C.3c}$$

These relations can be re-written in a compact form

$$\mathcal{L}\begin{pmatrix}\partial_{\xi_x}\mathbf{U}_c(\boldsymbol{\xi})\\ \partial_{\xi_y}\mathbf{U}_c(\boldsymbol{\xi})\\ \partial_{\tilde{\varphi}}\mathbf{U}_c(\boldsymbol{\xi})\end{pmatrix}=\begin{pmatrix}-\omega_0\,\partial_{\xi_y}\mathbf{U}_c(\boldsymbol{\xi})\\ \omega_0\,\partial_{\xi_x}\mathbf{U}_c(\boldsymbol{\xi})\\ \mathbf{v}_0\times\partial_{\tilde{\varphi}}\mathbf{U}_c(\boldsymbol{\xi})\end{pmatrix}=\begin{pmatrix}0 & -\omega_0 & 0\\ \omega_0 & 0 & 0\\ v_y^0 & -v_0^x & 0\end{pmatrix}\begin{pmatrix}\partial_{\xi_x}\mathbf{U}_c(\boldsymbol{\xi})\\ \partial_{\xi_y}\mathbf{U}_c(\boldsymbol{\xi})\\ \partial_{\tilde{\varphi}}\mathbf{U}_c(\boldsymbol{\xi})\end{pmatrix}. \tag{C.4}$$

The adjoint operator $\mathcal{L}^\dagger$ to $\mathcal{L}$ is defined with respect to the standard inner product in two-dimensional function space

$$\langle\mathbf{u},\mathcal{L}\mathbf{v}\rangle=\left\langle\mathcal{L}^\dagger\mathbf{u},\mathbf{v}\right\rangle\quad\text{with}\quad\langle\mathbf{u},\mathbf{v}\rangle=\int_{-\infty}^{\infty}\int_{-\infty}^{\infty}\mathrm{d}^2\mathbf{r}\overline{\mathbf{u}}^T(\mathbf{r})\,\mathbf{v}(\mathbf{r}), \tag{C.5}$$

where $\overline{\mathbf{u}}$ denotes complex conjugation; yielding

$$\mathcal{L}^\dagger=\mathbb{D}\Delta_{\boldsymbol{\xi}}-\omega_0\partial_{\tilde{\varphi}}-(\mathbb{A}(-\omega_0 t)\mathbf{v}_0)\cdot\nabla_{\boldsymbol{\xi}}+\mathcal{D}\mathbf{R}(\mathbf{U}_c(\boldsymbol{\xi}))^T. \tag{C.6}$$

Next, we introduce the so-called *response functions* $\mathbf{W}_i^\dagger(\boldsymbol{\xi})$, $i\in\{\xi_x,\xi_y,\tilde{\varphi}\}$. Although the latter do not coincide with the eigenfunctions of $\mathcal{L}^\dagger$ to eigenvalue zero, they are closely related to these. The response functions are also not identical to $\mathbf{W}_i$, $i\in\{\xi_x,\xi_y,\tilde{\varphi}\}$ because $\mathcal{L}$ is in general not self-adjoint. Regarding the Goldstone modes and response functions, one can distinguish three cases corresponding to (i) stationary solutions, (ii) traveling localized patterns like spots, and (iii) rotating solutions as *e.g.* spiral waves.

(i) For stationary, immobile solutions with $v_0^x=v_0^y=\omega_0=0$, all Goldstone-modes $\partial_i\mathbf{U}_c$, $i\in\{\xi_x,\xi_y,\tilde{\varphi}\}$, are ordinary eigenfunctions of $\mathcal{L}$ to eigenvalue $\lambda_0=0$. Additionally, the response functions are also ordinary eigenfunctions of $\mathcal{L}^\dagger$ to $\lambda_0=0$. For stationary patterns, $\mathcal{L}$ can be expressed by the product of a diagonal square matrix $\mathbb{M}$ and a self-adjoint matrix $\mathbb{L}$, $\mathcal{L}=\mathbb{M}\mathbb{L}$. Then, the eigenfunction $\mathbf{W}_i^\dagger$ are determined by the relation $\mathbf{W}_i^\dagger=\mathbb{M}^{-1}\partial_i\mathbf{U}_c$, $i\in\{\xi_x,\xi_y,\tilde{\varphi}\}$, for a given Goldstone mode $\partial_i\mathbf{U}_c$ [18].

(ii) For traveling localized patterns with $\omega_0=0$, both translational Goldstone modes $\partial_{\xi_x}\mathbf{U}_c$ and $\partial_{\xi_y}\mathbf{U}_c$ are ordinary eigenfunctions of $\mathcal{L}$ to $\lambda_0=0$. Similar, the response functions $\mathbf{W}_{\xi_x}^\dagger$ and $\mathbf{W}_{\xi_y}^\dagger$ are determined by $\mathcal{L}^\dagger\mathbf{W}_i^\dagger=0$, $i\in\{\xi_x,\xi_y\}$. On the other hand, the rotational Goldstone mode $\partial_{\tilde{\varphi}}\mathbf{U}_c$ is a generalized eigenfunction of rank $k=2$ to eigenvalue 0 such that $\mathcal{L}^2\partial_{\tilde{\varphi}}\mathbf{U}_c=0$ or $\mathcal{L}\partial_{\tilde{\varphi}}\mathbf{U}_c=v_0^y\partial_{\xi_x}\mathbf{U}_c-v_0^x\partial_{\xi_y}\mathbf{U}_c$. In a similar fashion, the corresponding rotational response function can be obtained as a solution of $\mathcal{L}^\dagger\mathbf{W}_{\tilde{\varphi}}^\dagger=v_0^y\mathbf{W}_{\xi_x}^\dagger-v_0^x\mathbf{W}_{\xi_y}^\dagger$.

(iii) In the case of solely rotating solutions with $\mathbf{v}_0=\mathbf{0}$, only the rotational Goldstone mode $\partial_{\tilde{\varphi}}\mathbf{U}_c(\boldsymbol{\xi})$ is an usual eigenfunction of $\mathcal{L}$ to eigenvalue zero, $\mathcal{L}\partial_{\tilde{\varphi}}\mathbf{U}_c(\boldsymbol{\xi})=0$. The same holds for the adjoint operator and the rotational response function, *i.e.*, $\mathcal{L}^\dagger\mathbf{W}_{\tilde{\varphi}}^\dagger(\boldsymbol{\xi})=0$. Although the translational Goldstone modes $\partial_i\mathbf{U}_c$, $\{\xi_x,\xi_y\}$ are not eigenfunctions of $\mathcal{L}$, linear combinations of them, viz. $\mathbf{Y}_\mp(\boldsymbol{\xi})=\pm i\partial_{\xi_x}\mathbf{U}_c+\partial_{\xi_y}\mathbf{U}_c$, yield eigenfunctions to eigenvalues $\lambda_{\pm1}=\pm i\omega_0$, $\mathcal{L}\mathbf{Y}_\mp(\boldsymbol{\xi})=\pm i\omega_0\mathbf{Y}_\mp(\boldsymbol{\xi})$. Since eigenvalues of $\mathcal{L}$ and the adjoint operator $\mathcal{L}^\dagger$ are complex conjugate to each other, there must be corresponding eigenfunctions $\mathbf{Y}_\mp^\dagger(\boldsymbol{\xi})$ to the adjoint operator $\mathcal{L}^\dagger$, $\mathcal{L}^\dagger\mathbf{Y}_\mp^\dagger(\boldsymbol{\xi})=\pm i\omega_0\mathbf{Y}_\mp^\dagger(\boldsymbol{\xi})$.

C.2 Multiple scale perturbation expansion

In order to quantify the response of the stable spot pattern $\mathbf{U}_c$ to an external control $\mathbf{f}(\mathbf{U}(\mathbf{r},t),\mathbf{r},t)$ in (A.1a), we perform a multiple scale perturbation expansion in the small time scale $T=\epsilon t$. The time derivative is transformed as $\partial_t\to\partial_t+\epsilon\partial_T$ and from now on t and T are treated as two independent variables. The state $\mathbf{U}$ is now a function of this new time scale while the perturbation $\mathbf{f}$ depends on T only through $\mathbf{U}$, *i.e.*,

$\mathbf{U} = \mathbf{U}(\mathbf{r}, t, T)$ and $\mathbf{f} = \mathbf{f}(\mathbf{U}(\mathbf{r}, t, T), \mathbf{r}, t)$. Introducing this time scale, the perturbed RDS (2a) reads as

$$\partial_t \mathbf{U}(\mathbf{r}, t, T) + \epsilon \partial_T \mathbf{U}(\mathbf{r}, t, T) = \mathbb{D}\Delta\mathbf{U} + \mathbf{R}(\mathbf{U}(\mathbf{r}, t, T)) + \mathbb{B}\,\mathbf{f}(\mathbf{U}(\mathbf{r}, t, T)\,\mathbf{r}, t). \tag{C.7}$$

If the perturbations $\mathbb{B}\,\mathbf{f}$ are weak, the latter mainly causes translation and rotation of the TW pattern. Thus, we define the current position and orientation by $\mathbf{\Phi}(t, T) = (\Phi_x(t, T), \Phi_y(t, T))^T$ and $\Phi_\varphi(t, T)$, respectively. We stress that both $\mathbf{\Phi}$ and Φ_φ depend on both time scales. Then, we can introduce the new co-moving coordinate

$$\tilde{\mathbf{r}} = \tilde{\mathbf{r}}(\mathbf{r}, t, T) = \mathbb{A}(-\Phi_\varphi(t, T)) \cdot (\mathbf{r} - \mathbf{\Phi}(t, T)), \tag{C.8}$$

which transforms (C.7) into

$$\begin{aligned}
\partial_t \mathbf{U}(\tilde{\mathbf{r}}, t, T) + \epsilon \partial_T \mathbf{U}(\tilde{\mathbf{r}}, t, T) &= \mathbb{D}\Delta\mathbf{U}(\tilde{\mathbf{r}}, t, T) + \mathbf{R}(\mathbf{U}(\tilde{\mathbf{r}}, t, T)) \\
&+ \mathbb{B}\,\mathbf{f}(\mathbf{U}(\tilde{\mathbf{r}}, t, T), \mathbb{A}(\Phi_\varphi(t, T)) \cdot \tilde{\mathbf{r}} + \mathbf{\Phi}(t, T), t) + \partial_t \Phi_\varphi(t, T)\, \partial_{\tilde{\varphi}} \mathbf{U}(\tilde{\mathbf{r}}, t, T) \\
&+ (\mathbb{A}(-\Phi_\varphi(t, T))\, \partial_t \mathbf{\Phi}(t, T)) \cdot \nabla_{\tilde{\mathbf{r}}} \mathbf{U}(\tilde{\mathbf{r}}, t, T) + \epsilon \partial_T \Phi_\varphi(t, T)\, \partial_{\tilde{\varphi}} \mathbf{U}(\tilde{\mathbf{r}}, t, T) \\
&+ \epsilon (\mathbb{A}(-\Phi_\varphi(t, T))\, \partial_T \mathbf{\Phi}(t, T)) \cdot \nabla_{\tilde{\mathbf{r}}} \mathbf{U}(\tilde{\mathbf{r}}, t, T).
\end{aligned} \tag{C.9}$$

Now, we suppose that the perturbed solution to (C.9) can be composed of the unperturbed, stable TW solution $\mathbf{U}_c$ and a function $\tilde{\mathbf{v}}$

$$\mathbf{U} = \mathbf{U}_c + \epsilon \tilde{\mathbf{v}}. \tag{C.10}$$

Thereby, $\tilde{\mathbf{v}}$ is assumed to be orthogonal to the response functions $\mathbf{W}_i^\dagger$, $\langle \mathbf{W}_i^\dagger, \tilde{\mathbf{v}} \rangle = 0$. Using this ansatz, we expand the solution in orders of ϵ and get in leading order $\mathcal{O}(1)$

$$\begin{aligned}
\mathbb{D}\Delta\mathbf{U}_c(\tilde{\mathbf{r}}) &+ \partial_t \Phi_\varphi(t, T)\, \partial_{\tilde{\varphi}} \mathbf{U}_c(\tilde{\mathbf{r}}) \\
&+ (\mathbb{A}(-\Phi_\varphi(t, T))\, \partial_t \mathbf{\Phi}(t, T)) \cdot \nabla_{\tilde{\mathbf{r}}} \mathbf{U}_c(\tilde{\mathbf{r}}) + \mathbf{R}(\mathbf{U}_c(\tilde{\mathbf{r}})) = 0.
\end{aligned} \tag{C.11}$$

From the comparison with (C.1) it becomes immediately clear that the functions Φ_φ and $\mathbf{\Phi}$ must behave like

$$\mathbf{\Phi}(t, T) = \mathbf{v}_0 t + \mathbf{p}(T) + \mathcal{O}(\epsilon), \tag{C.12}$$

$$\Phi_\varphi(t, T) = \omega_0 t + p_\varphi(T) + \mathcal{O}(\epsilon), \tag{C.13}$$

with $\mathbf{p}(T) = (p_x(T), p_y(T))^T$ and the p_φ depend only on the slow time scale T. Using the last result, we get in order $\mathcal{O}(\epsilon)$

$$\begin{aligned}
\partial_t \tilde{\mathbf{v}}(\tilde{\mathbf{r}}, t, T) - \mathcal{L}\tilde{\mathbf{v}} =& \partial_T \Phi_\varphi(t, T)\, \partial_{\tilde{\varphi}} \mathbf{U}_c(\tilde{\mathbf{r}}) + (\mathbb{A}(-\Phi_\varphi(t, T))\, \partial_T \mathbf{\Phi}(t, T)) \cdot \nabla_{\tilde{\mathbf{r}}} \mathbf{U}_c(\tilde{\mathbf{r}}) \\
&+ \mathbb{B}\,\mathbf{f}(\mathbf{U}_c(\tilde{\mathbf{r}}, t, T), \mathbb{A}(\Phi_\varphi(t, T))\, \tilde{\mathbf{r}} + \mathbf{\Phi}(t, T), t),
\end{aligned} \tag{C.14}$$

where $\mathcal{L}$ denotes the linear stability operator of $\mathbf{U}_c$, (C.2). Equation (C.14) is a linear PDE with an inhomogeneity on the r.h.s.. Next, we multiply from the left with one of the three response function $\mathbf{W}_i^\dagger(\tilde{\mathbf{r}})$, $i \in \{x, y, \varphi\}$ and invoke the relations $\langle \mathbf{W}_i^\dagger, \partial_t \tilde{\mathbf{v}} \rangle = \partial_t \langle \mathbf{W}_i^\dagger, \tilde{\mathbf{v}} \rangle = 0$ and $\langle \mathbf{W}_i^\dagger, \mathcal{L}\tilde{\mathbf{v}} \rangle = \langle \mathcal{L}^\dagger \mathbf{W}_i^\dagger, \tilde{\mathbf{v}} \rangle = 0$ to eliminate the l.h.s.

$$\begin{aligned}
0 = \partial_T \Phi_\varphi(t, T) \left\langle \mathbf{W}_i^\dagger(\tilde{\mathbf{r}}), \partial_{\tilde{\varphi}} \mathbf{U}_c(\tilde{\mathbf{r}}) \right\rangle &+ (\mathbb{A}(-\Phi_\varphi(t, T)) \cdot \partial_T \mathbf{\Phi}(t, T)) \cdot \langle \mathbf{W}_i^\dagger(\tilde{\mathbf{r}}), \nabla_{\tilde{\mathbf{r}}} \mathbf{U}_c(\tilde{\mathbf{r}}) \rangle \\
+ \left\langle \mathbf{W}_i^\dagger(\tilde{\mathbf{r}}), \mathbb{B}\,\mathbf{f}(\mathbf{U}_c(\tilde{\mathbf{r}}, t, T), \mathbb{A}(\Phi_\varphi(t, T))\, \tilde{\mathbf{r}} + \mathbf{\Phi}(t, T), t) \right\rangle.
\end{aligned} \tag{C.15}$$

Introducing $\mathbb{A}_z(\alpha) = [\cos(\alpha), -\sin(\alpha), 0; \sin(\alpha), \cos(\alpha), 0; 0, 0, 1]$ for the clockwise rotation matrix around the z-axes in 3D, (C.15) can be written as

$$\mathcal{C}\mathbb{A}^z\left(-\Phi_\varphi\left(t,T\right)\right)\partial_T\begin{pmatrix}\Phi_x(t,T)\\ \Phi_y(t,T)\\ \Phi_\varphi(t,T)\end{pmatrix} = -\begin{pmatrix}\langle\mathbf{W}_x^\dagger, \mathbb{B}\,\mathbf{f}\rangle\\ \langle\mathbf{W}_y^\dagger, \mathbb{B}\,\mathbf{f}\rangle\\ \langle\mathbf{W}_\varphi^\dagger, \mathbb{B}\,\mathbf{f}\rangle\end{pmatrix}, \tag{C.16}$$

where $\mathcal{C}_{ij} = \langle\mathbf{W}_i^\dagger, \partial_j\mathbf{U}_c\rangle$, $i \in \{x, y, \varphi\}$.

Because any dependence on the second time scale T appears only in the general position vector $\mathbf{\Xi}\left(t,T\right) = \left(\Phi_x\left(t,T\right), \Phi_y\left(t,T\right), \Phi_\varphi\left(t,T\right)\right)^T$, we can eliminate the second time scale T with one last step. Therefore, we introduce the single time scale function $\mathbf{\Xi}\left(t\right) = \mathbf{\Xi}\left(t, \epsilon\, t\right)$, yielding $\partial_t\mathbf{\Xi}\left(t\right) = \partial_t\mathbf{\Xi}\left(t,T\right) + \epsilon\partial_T\mathbf{\Xi}\left(t,T\right)$. Finally, we derive the following equations of motion for a localized TW pattern under the impact of a weak perturbation $\mathbf{f}$ using (C.12), (C.13), and (C.16)

$$\frac{\mathrm{d}}{\mathrm{d}t}\begin{pmatrix}\Phi_x(t)\\ \Phi_y(t)\\ \Phi_\varphi(t)\end{pmatrix} = \begin{pmatrix}v_0^x\\ v_0^y\\ \omega_0\end{pmatrix} - \epsilon\mathbb{A}^z\left(\Phi_\varphi\left(t\right)\right)\mathcal{C}^{-1}\begin{pmatrix}\langle\mathbf{W}_x^\dagger, \mathbb{B}\,\mathbf{f}\rangle\\ \langle\mathbf{W}_y^\dagger, \mathbb{B}\,\mathbf{f}\rangle\\ \langle\mathbf{W}_\varphi^\dagger, \mathbb{B}\,\mathbf{f}\rangle\end{pmatrix}, \tag{C.17}$$

with

$$\langle\mathbf{W}_i^\dagger, \mathbb{B}\,\mathbf{f}\rangle = \int_{-\infty}^{\infty}\int_{-\infty}^{\infty}\mathrm{d}^2\mathbf{r}\,\overline{\mathbf{W}_i^\dagger}^T\left(\mathbb{A}\left(-\Phi_\varphi\left(t\right)\right)\left(\mathbf{r} - \mathbf{\Phi}\left(t\right)\right)\right)\mathbb{B}\,\mathbf{f}\left(\mathbf{r},t\right). \tag{C.18}$$

C.3 Inverse problem – solving for the control

Folllowing [26], now we consider the inverse problem and view (C.17) as a conditional equation for the control $\mathbf{f}$. The latter is assumed to be a linear superposition of Goldstone modes

$$\epsilon\mathbb{B}\,\mathbf{f}(\mathbf{r},t) = K_1\partial_x\mathbf{U}_c\left(\boldsymbol{\xi}(t)\right) + K_2\partial_y\mathbf{U}_c\left(\boldsymbol{\xi}(t)\right) + K_3\partial_\varphi\mathbf{U}_c\left(\boldsymbol{\xi}(t)\right), \tag{C.19}$$

where $\mathbf{U}_c$ is evaluated at the presumed position in space $\bar{\boldsymbol{\xi}}(t) = \mathbb{A}\left(-\Phi_\varphi\left(t\right)\right)\left(\mathbf{r} - \mathbf{\Phi}\left(t\right)\right)$. Plugging (C.19) into $\left\langle\mathbf{W}_i^\dagger, \mathbb{B}\,\mathbf{f}\right\rangle$, $i \in \{x, y, \varphi\}$, one gets

$$\epsilon\begin{pmatrix}\langle\mathbf{W}_x^\dagger, \mathbb{B}\,\mathbf{f}\rangle\\ \langle\mathbf{W}_y^\dagger, \mathbb{B}\,\mathbf{f}\rangle\\ \langle\mathbf{W}_\varphi^\dagger, \mathbb{B}\,\mathbf{f}\rangle\end{pmatrix} = \mathcal{C}\begin{pmatrix}K_1\\ K_2\\ K_3\end{pmatrix}, \tag{C.20}$$

and, hence, the expansion coefficients K_j are given as

$$\begin{pmatrix}K_1\\ K_2\\ K_3\end{pmatrix} = \mathbb{A}^z\left(-\Phi_\varphi\left(t\right)\right)\left[\begin{pmatrix}v_0^x\\ v_0^y\\ \omega_0\end{pmatrix} - \frac{\mathrm{d}}{\mathrm{d}t}\begin{pmatrix}\Phi_x(t)\\ \Phi_y(t)\\ \Phi_\varphi(t)\end{pmatrix}\right]. \tag{C.21}$$

Finally, we obtain the analytical expressions for Goldstone mode control $\mathbf{f}_{\mathrm{Gold}}$ based on asymptotic perturbation analysis

$$\mathbf{f}_{\mathrm{Gold}}(\mathbf{r},t) = \left[\left(\begin{pmatrix}v_0^x\\ v_0^y\\ \omega_0\end{pmatrix} - \mathbb{A}_z\left(-\Phi_\varphi(t)\right)\frac{\mathrm{d}}{\mathrm{d}t}\begin{pmatrix}\Phi_x(t)\\ \Phi_y(t)\\ \Phi_\varphi(t)\end{pmatrix}\right)\cdot\tilde{\nabla}_{\boldsymbol{\xi}}\right]\mathbf{U}_c(\boldsymbol{\xi})\Big|_{\boldsymbol{\xi}=\bar{\boldsymbol{\xi}}(t)}. \tag{C.22}$$

We stress that the derivatives $\tilde{\nabla}_{\boldsymbol{\xi}}\mathbf{U}_c$, with $\tilde{\nabla}_{\boldsymbol{\xi}} = (\partial_{\xi_x}, \partial_{\xi_y}, \partial_{\varphi})^T$, have to be calculated in the co-moving and co-rotation frame of reference and then evaluated at the currently presumed position of the pattern $\bar{\boldsymbol{\xi}}(t) = \mathbb{A}\left(-\Phi_{\varphi}(t)\right)\left(\mathbf{r} - \boldsymbol{\Phi}(t)\right)$.

Acknowledgements. We thank Alexander Ziepke for helpful discussions as well as for critical reading of the manuscript and acknowledge financial support from the German Science Foundation DFG through the SFB 910 "Control of Self-Organizing Nonlinear Systems".

Supplementary Material

The Supplementary Material is available at https://www.mmnp-journal.org/10.1051/mmnp/2021036 for the mmnp200326/olm.

References

[1] F.T. Arecchi, S. Boccaletti and P. Ramazza, Pattern formation and competition in nonlinear optics. *Phys. Rep.* **318** (1999) 1–83.
[2] W. Barthel, C. John and F. Tröltzsch, Optimal boundary control of a system of reaction diffusion equations. *Z. Angew. Math. und Mech.* **90** (2010) 966–982.
[3] I.V. Biktasheva, H. Dierckx and V.N. Biktashev, Drift of scroll waves in thin layers caused by thickness features: asymptotic theory and numerical simulations. *Phys. Rev. Lett.* **114** (2015) 068302.
[4] R. Buchholz, H. Engel, E. Kammann and F. Tröltzsch, On the optimal control of the Schlögl model. *Comput. Optim. Appl.* **56** (2013) 153–185.
[5] A.E. Bryson, Applied optimal control: optimization, estimation and control. CRC Press (1975).
[6] E. Casas, M. Mateos and A. Rösch, Improved approximation rates for a parabolic control problem with an objective promoting directional sparsity. *Comp. Opt. Appl.* **70** (2018) 239–266.
[7] E. Casas, C. Ryll and F. Tröltzsch, Sparse optimal control of the Schlögl and FitzHugh-Nagumo systems. *Comp. Meth. Appl. Math.* **13** (2013) 415–442.
[8] E. Casas, C. Ryll and F. Tröltzsch, Optimal control of a class of reaction diffusion equations. *Comput. Opt. Appl.* **70** (2018) 677–707.
[9] E. Casas, C. Ryll and F. Tröltzsch, Second order and stability analysis for optimal sparse control of the FitzHugh-Nagumo equation. *SIAM J. Control Optim.* **53** (2015) 2168–2202.
[10] J.-X. Chen, H. Zhang and Y.-Q. Li, Synchronization of a spiral by a circularly polarized electric field in reaction–diffusion systems. *J. Chem. Phys.* **130** (2009) 124510.
[11] S. Coombes, P. Beim Graben, R. Potthast and J. Wright, Neural Fields. Springer-Verlag Berlin Heidelberg (2014).
[12] S.M. Cox and P.C. Matthews, *J. Comp. Phys.* **176** (2002) 430–455.
[13] A. Doelman, P. van Heijster and T.J. Kaper, Pulse dynamics in a three-component system: existence analysis. *J. Dyn. Differ. Equ.* **21** (2009) 73–115.
[14] R. FitzHugh, Impulses and physiological states in theoretical models of nerve membrane. *Biophys. J.* **1** (1961) 445–466.
[15] E. Gilad, J. von Hardenberg, A. Provenzale, M. Shachak and E. Meron, Ecosystem engineers: from pattern formation to habitat creation. *Phys. Rev. Lett.* **93** (2004).
[16] S.V. Gurevich and R. Friedrich, Instabilities of localized structures in dissipative systems with delayed feedback. *Phys. Rev. Lett.* **110** (2013).
[17] S.V. Gurevich, S. Amiranashvili and H.-G. Purwins, Breathing dissipative solitons in three-component reaction–diffusion system. *Phys. Rev. E* **74** (2006) 066201.
[18] S. Gurevich, H. Bödeker, A. Moskalenko, A. Liehr and H.G. Purwins, *Physica D* **199** (2004) 115–128.
[19] G. Haas, M. Bär, I.G. Kevrekidis, P.B. Rasmussen, H.H. Rotermund and G. Ertl, *Phys. Rev. Lett.* **75** (1995) 3560.
[20] K.-H. Hoffmann, I. Lasiecka, G. Leugering, J. Sprekels and F. Tröltzsch, eds., *Optimal Control of Complex Structures*. Vol. 139 of *ISNM*. Birkhäuser Verlag (2002).
[21] K.-H. Hoffmann, G. Leugering and F. Tröltzsch, Optimal Control of Partial Differential Equations. Vol. 133 of *ISNM*. Birkhäuser Verlag (1998).
[22] B.S. Kerner and V.V. Osipov, Vol. 61 of Autosolitons: a new approach to problems of self-organization and turbulence. Springer Science & Business Media (2013).
[23] M. Kim, M. Bertram, M. Pollmann, A. von Oertzen, A.S. Mikhailov, H.H. Rotermund and G. Ertl, Controlling chemical turbulence by global delayed feedback: Pattern formation in catalytic CO oxidation on Pt(110). *Science* **292** (2001) 1357.
[24] C.R. Laing, W.C. Troy, B. Gutkin and G.B. Ermentrout, Multiple bumps in a neuronal model of working memory. *SIAM J. Appl. Math.* **63** (2002) 62–97.
[25] T. Le Goff, B. Liebchen and D. Marenduzzo, Pattern Formation in polymerizing actin flocks: spirals, spots, and waves without nonlinear chemistry. *Phys. Rev. Lett.* **117** (2016) 238002.

[26] J. Löber and H. Engel, Controlling the position of traveling waves in reaction–diffusion systems. *Phys. Rev. Lett.* **112** (2014) 148305.
[27] J. Löber, R. Coles, J. Siebert, H. Engel and E. Schöll, Control of chemical wave propagation, in Engineering of Chemical Complexity II, edited by A. Mikhailov and G. Ertl. World Scientific, Singapore (2015).
[28] J. Löber, Stability of position control of traveling waves in reaction–diffusion systems. *Phys. Rev. E* **89** (2014) 062904.
[29] J. Löber, S. Martens and H. Engel, Shaping wave patterns in reaction–diffusion systems. *Phys. Rev. E* **90** (2014) 062911.
[30] O. Lüthje, S. Wolff and G. Pfister, Control of chaotic Taylor-Couette flow with time-delayed feedback. *Phys. Rev. Lett.* **86** (2001) 1745–1748.
[31] J. Löber, Control of reaction–diffusion systems. Springer International Publishing, Cham (2017) 195–220.
[32] B. Marwaha and D. Luss, *Chem. Eng. Sci.* **58** (2003) 733–738.
[33] A. Mikhailov and K. Showalter, Control of waves, patterns and turbulence in chemical systems. *Phys. Rep.* **425** (2006) 79–194.
[34] A. Mikhailov, L. Schimansky-Geier and W. Ebeling, Stochastic motion of the propagating front in bistable media. *Phys. Lett. A* **96** (1983) 453–456.
[35] Y. Nishiura, T. Teramoto and K.-I. Ueda, Scattering of traveling spots in dissipative systems. *Chaos* **15** (2005) 047509.
[36] Y. Nishiura, T. Teramoto and X. Yuan, Heterogeneity-induced spot dynamics for a three-component reaction–diffusion system. *Comm. Pure Appl. Anal.* **11** (2011) 307–338.
[37] V. Odent, E. Louvergneaux, M.G. Clerc and I. Andrade-Silva, Optical wall dynamics induced by coexistence of monostable and bistable spatial regions. *Phys. Rev. E* **94** (2016) 052220.
[38] T. Pierre, G. Bonhomme and A. Atipo, Controlling the chaotic regime of nonlinear ionization waves using the time-delay autosynchronization method. *Phys. Rev. Lett.* **76** (1996) 2290–2293.
[39] H.-G. Purwins, H.U. Bödeker and A.W. Liehr, Dissipative solitons in reaction–diffusion systems. *Dissipative solitons*. Springer (2005) 267–308.
[40] H.-G. Purwins, H. Bödeker and S. Amiranashvili, Dissipative solitons. *Adv. Phys.* **59** (2010) 485–701.
[41] L. Qiao, X. Li, I.G. Kevrekidis, C. Punckt and H.H. Rotermund, Enhancement of surface activity in CO oxidation on Pt(110) through spatiotemporal laser actuation. *Phys. Rev. E* **77** (2008) 036214.
[42] C. Ryll, J. Löber, S. Martens, H. Engel and F. Tröltzsch, Analytical, optimal, and sparse optimal control of traveling wave solutions to reaction–diffusion systems, in Control of Self-Organizing Nonlinear Systems, edited by E. Schöll, S.H.L. Klapp and P. Hövel. Springer (2016) 189–210.
[43] T. Sakurai, E. Mihaliuk, F. Chirila and K. Showalter, Design and control of wave propagation patterns in excitable media. *Science* **296** (2002) 2009–2012.
[44] J. Schlesner, V. Zykov and H. Engel, Feedback-mediated control of hypermeandering spiral waves, in Handbook of Chaos Control. Wiley-VCH Verlag (2008) 591–607.
[45] A. Schrader, M. Braune and H. Engel, Dynamics of spiral waves in excitable media subjected to external periodic forcing. *Phys. Rev. E* **52** (1995) 98.
[46] O. Steinbock, V.S. Zykov and S.C. Müller, Control of spiral-wave dynamics in active media by periodic modulation of excitability. *Nature* **366** (1993) 322–324.
[47] J.S. Taube and J.P. Bassett, Persistent neural activity in head direction cells. *Cereb. Cortex* **13** (2003) 1162–1172.
[48] S. Totz, J. Löber, J.F. Totz and H. Engel, Control of transversal instabilities in reaction–diffusion systems. *NJP* **20** (2018) 053034.
[49] P. van Heijster, A. Doelman and T.J. Kaper, Pulse dynamics in a three-component system: stability and bifurcations. *Physica D* **237** (2008) 3335–3368.
[50] V.K. Vanag and I.R. Epstein, Design and control of patterns in reaction–diffusion systems. *Chaos* **18** (2008) 026107.
[51] V.K. Vanag and I.R. Epstein, Localized patterns in reaction–diffusion systems. *Chaos* **17** (2007) 037110.
[52] G.A. Viswanathan, M. Sheintuch and D. Luss, Transversal hot zones formation in catalytic packed-bed reactors. *Ind. Eng. Chem. Res.* **47** (2008) 7509–7523.
[53] J. Wolff, A.G. Papathanasiou, I.G. Kevrekidis, H.H. Rotermund and G. Ertl, Spatiotemporal addressing of surface activity. *Science* **294** (2001) 134–137.
[54] J. Wolff, A.G. Papathanasiou, H.H. Rotermund, G. Ertl, X. Li and I.G. Kevrekidis, Gentle dragging of reaction waves. *Phys. Rev. Lett.* **90** (2003) 018302.
[55] L. Yang, A.M. Zhabotinsky and I.R. Epstein, Jumping solitary waves in an autonomous reaction–diffusion system with subcritical wave instability. *Phys. Chem. Chem. Phys.* **8** (2006) 4647–4651.
[56] A. Ziepke, S. Martens and H. Engel, Control of nonlinear wave solutions to neural field equations. arXiv:1806.10938 (2018).
[57] A. Ziepke, S. Martens and H. Engel, Wave propagation in spatially modulated tubes. *J. Chem. Phys.* **145** (2016) 094108.
[58] V.S. Zykov, G. Bordiougov, H. Brandtstädter, I. Gerdes and H. Engel, Periodic forcing and feedback control of nonlinear lumped oscillators and meandering spiral waves. *Phys. Rev. E* **68** (2003) 016214.
[59] V.S. Zykov, G. Bordiougov, H. Brandtstädter, I. Gerdes and H. Engel, Global control of spiral wave dynamics in an excitable domain of circular and elliptical shape. *Phys. Rev. Lett.* **92** (2004) 018304.